Ultrasound-induced dense granular flows: a two-time scale modeling

Hugo A. Martin, Anne Mangeney, Xiaoping Jia, Bertrand Antti Maury, Aline Lefebvre-Lepot, Yvon Maday, Paul Dérand

To cite this version:

Hugo A. Martin, Anne Mangeney, Xiaoping Jia, Bertrand Antti Maury, Aline Lefebvre-Lepot, et al.. Ultrasound-induced dense granular flows: a two-time scale modeling. 2024. hal-04454075

HAL Id: hal-04454075
https://hal.science/hal-04454075

Preprint submitted on 12 Feb 2024

Ultrasound-induced dense granular flows: a two-time scale modeling

H. A. Martin[1,2] †, A. Mangeney[1,3], X. Jia[4] ‡, B. Maury[5,6], A. Lefebvre-Lepot[7], Y. Maday[2,3], and P. Dérand[4]

[1]Institut de Physique du Globe de Paris, Université Paris Cité, CNRS, F-75005 Paris, France

[2]Laboratoire Jacques-Louis Lions (LJLL), Sorbonne Université, CNRS, Université Paris Cité, F-75005 Paris, France

[3]Institut Universitaire de France (IUF), 75231 Paris Cedex 05, France

[4]Institut Langevin, ESPCI Paris, Université PSL, CNRS, France

[5]Département de Mathématiques Appliquées, École Normale Supérieure, Université PSL, Paris, France

[6]Laboratoire de Mathématiques d'Orsay, Université Paris-Saclay, 91405 Orsay Cedex, France

[7]Fédération de Mathématiques de CentraleSupélec, CNRS FR-3487, CentraleSupélec, Université Paris-Saclay, Saclay, France

Understanding the mechanisms behind the remote triggering of landslides by seismic waves at micro-strain amplitude is essential for quantifying seismic hazards. Granular materials provide a relevant model system to investigate landslides within the unjamming transition framework, from solid to liquid states. Furthermore, recent laboratory experiments have revealed that ultrasound-induced granular avalanches can be related to a reduction in the interparticle friction through shear acoustic lubrication of contacts. However, investigating slip at the scale of grain contacts within an optically opaque granular medium remains a challenging issue. Here, we propose an original coupling model and numerically investigate 2D dense granular flows triggered by basal acoustic waves. We model the triggering dynamics at two separated time-scales—one for grain motion (milliseconds) and the other for ultrasound (10 microseconds)—relying the computation of vibrational modes with a discrete element method through the reduction of the local friction. We show that ultrasound predominantly propagates through the strong-force chains, while the ultrasound-induced decrease of interparticle friction occurs in the weak contact forces perpendicular to the strong-force chains. This interparticle-friction reduction initiates local rearrangements at the grain scale that eventually lead to a continuous flow through a percolation process at the macroscopic scale—with a delay depending the proximity to the failure. Consitent with the experiment, we show that ultrasound-induced flow appears more uniform in space than pure gravity-driven flow, indicating the role of an effective temperature by ultrasonic vibration.

Key words: Dry granular material, Waves in random media, Computational methods

---

† Email address for correspondence: martin_hugo@ymail.com
‡ Email address for correspondence: xiaoping.jia@espci.fr

1. Introduction

The shear instability in a granular medium is involved in many natural hazards such as seismic fault slips and landslides. One of important and challenging issue in seismic hazard investigation is to understand how small-amplitude seismic waves (of the order of micro-strain) can trigger remotely earthquakes from hundreds of km (Gomberg *et al.* 2001; Hill *et al.* 1993) or more locally landslides around a volcano (Keefer 2002). Recent observations showed that perturbations from local foreshock activity are probably a part of the earthquake nucleation process (Bouchon *et al.* 2013) and that large rockfall events and avalanches can be triggered by volcanic seismicity (Durand *et al.* 2018). Dynamic stress from seismic waves can destabilize granular solids and force failure earlier in time relative to an unperturbed fault or slope. Indeed, static and dynamic properties of dense granular media are determined by inhomogeneous contact force networks, exhibiting multiple metastable configurations. Sound waves propagating from grain to grain provide not only a unique probe of such optically opaque networks (Liu & Nagel 1992; Jia *et al.* 1999) but also a controlled perturbation via vibration-induced softening and dissipation (Johnson & Jia 2005; Jia *et al.* 2011). Granular media undergo a transition from a jammed solid state to a flowing liquid state when the external shear exceeds the static yield stress (Fig. 1(a, b)).

Previous works pointed this transition as bifurcation phenomenon (Jaeger *et al.* 1990; Quartier *et al.* 2000; Baldassarri *et al.* 2006; Dijksman *et al.* 2011), similar to solid friction at multicontact interfaces (Baumberger & Caroli 2006) described by the rate and state friction law (Marone 1998; Scholz 2019). Here, the friction coefficient is defined as $\mu = \tau/\sigma_n$, as the ratio of the shear stress normalized by the normal stress from which the static and dynamic coefficients of friction $\mu_{s,d} = \tau_{s,d}/\sigma_n$ follow, where τ_s is the static friction stress at yield while τ_d is the dynamic friction stress. In the inclined plane geometry considered in this article (Fig. 1(a)), we have $\mu = \tan\theta$ and $\mu_s = \tan\theta_m$, with θ_m the (maximum) angle of avalanche. The angle of repose θ_r being a few percent lower than θ_m (Pouliquen & Renaut 1996; Daerr & Douady 1999; Coussot *et al.* 2002; Wyart 2009) corresponds to the dynamic friction $\mu_d = \tan\theta_r$ at the minimum shear load (Fig. 1(b)). It has been shown (Baumberger & Caroli 2006; Nasuno *et al.* 1997; Bureau *et al.* 2001; Parteli *et al.* 2005) that for shear forces far below the static threshold $\mu \ll \mu_s$, both granular layers and rough solid interfaces respond elastically as shown in Fig. 1(b), in the jammed state (region I). For $\mu \lesssim \mu_s$ a shear lower than the threshold, nonlinear response occurs with creep-like irreversible motion. For $\mu \gtrsim \mu_s$, the system yields and starts to slide or flow over a transient characteristic distance (Marone 1998; Scholz 2019; Baumberger & Caroli 2006) before reaching the steady flow region II/III at a velocity V or shear rate $\dot{\gamma}$ imposed by the load.

The possible failure of a granular medium, such as a sand pile, caused by external vibrations, has been known for a long time in engineering and geophysical applications, however a unified physical description still lacks. The vibrations considered are most of the time of *large amplitude* $U_0 \gtrsim d$ with d the grain size and *low frequency* $f < f_0$, where f_0 is a characteristic frequency determined by the stiffness of interfacial contacts (Bureau *et al.* 2001). The amount of shaking is usually estimated by the reduced peak acceleration of the grain $\Gamma = a/g$ with a the instantaneous acceleration and g the gravity. When $\Gamma > 1$, vertical vibrations cancel almost normal forces exerting on the grain (confined under gravity) and modify consequently the spatial arrangement of grains, resulting in phenomena such as compaction, convection, shear banding, to mention a few (Jaeger *et al.* 1989; Clement & Rajchenbach 1991; D'Anna *et al.* 2003). This is similar to the oscillation effect on the normal stress facilitating sliding (Zaloj *et al.* 1999; Cochard *et al.* 2003) and also to the scenario of the acoustic lubrication in a confined continuous medium. In this scenario, the acoustic pressure $p_a = (\rho c)v_a$, with c the sound speed and v_a the vibration velocity, is expected to

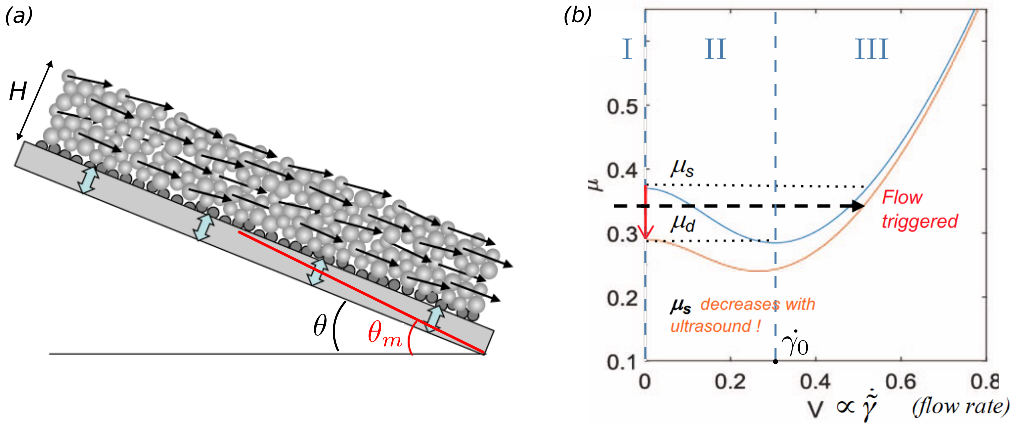

Figure 1: *(a)* 2D schematic illustration of granular flows triggered by small-amplitude ultrasonic or seismic vibration (indicated by double arrows) where the granular layer of thickness H is deposited on a slope at angle θ below the maximum angle of stability θ_m. The inertial flow triggered by ultrasonic vibration is mostly uniform and continuous. *(b)* Sketch of the normalized stress-strain rate relation in a sheared granular medium: static state (V = 0), unstable flow (velocity-weakening) and stable flow (velocity strengthening). Under a shear μ between μ_s and μ_d, the metastable state can be switched abruptly to a flowing state by acoustic perturbation (lubrication).

temporally relieve the pressure of the overburden, thereby decreasing the yield stress (Melosh 1996).

However, the above scenarios, involving large-amplitude vibrations, cannot explain the dynamic earthquake triggering by seismic waves at micro- and nano-strain amplitude (Scholz 2019; Gomberg *et al.* 2001), nor the laboratory experiments using nanometer-amplitude ultrasound to soften the material modulus by 30 % via nonlinear dynamics (Johnson & Jia 2005; Jia *et al.* 2011). Also, some modifications of the stick-slip cycle by ultrasound remain unexplained (Johnson *et al.* 2008). In these situations, the oscillation frequency of ultrasound $f \geqslant 40\,\mathrm{kHz}$ is high compared to the characteristic frequency of $f_0 \simeq 5\,\mathrm{kHz}$ in millimeter-thick granular layers (Baumberger & Caroli 2006; Bureau *et al.* 2001) so that grains cannot have enough inertial normal motion to suppress the weight of the overburden. On the other hand, for a nanometer ultrasonic vibration, the collision-like pressure estimated as $p_c \simeq 10^{-4}\,\mathrm{Pa} \ll \sigma_n$ ($\simeq 10\,\mathrm{Pa}$) is too small to be considered.

Recently, it was evidenced by lab experiments (Leópoldès *et al.* 2020) that the triggering of granular instabilities by *small-amplitude* ($U_0/d \simeq 10^{-5}$) and *high-frequency* ($f = 70\,\mathrm{kHz}$) ultrasound waves can be explained by acoustic shear lubrication of grain contacts. This interparticle friction reduction consequently lowers the effective friction coefficient on the macroscopic scale and triggers the granular flow at an inclined angle below θ_m (Fig. 1(b)) without causing the rearrangement of grain positions, . However, it remains unclear how such local effects could give rise to collective motion and also their possible delay of response (Durand *et al.* 2018). In particular, the micro processes of triggering remain poorly understood, as small-amplitude ultrasound does not induce grain displacement *per se* at the relevant length scale (i.e., grain diameter d) during avalanches.

In this article, we address these questions by presenting numerical simulations of the onset of flows of a granular layer initially static on an inclined plane, triggered by ultrasound applied from the basal plane. To do so, we propose an original coupling model, relying on a time-scale separation, with one time scale representing the grain-scale dynamics (called the *grain-motion time scale*) and the other representing the ultrasonic vibration in the granular medium (called the *vibration time scale*). At the *vibration time scale*, the granular packing (particles) is considered quasi-static. Therefore, our methodology involves coupling a Discrete Element Model (DEM) for grain flows with a mass-spring model (network) for wave vibration. The latter is investigated in the steady (harmonic) regime through *vibrational (eigen) modes*. Once the amplitudes of the vibration field are computed, the acoustic lubrication effect on the (entire) granular medium is taken into account through modifications of the interparticle friction coefficients, according to the *Mindlin model* (Leópoldès *et al.* 2020). To our knowledge, this is the first time such a coupling numerical methodology has been employed to study the acoustic lubrication effect on the granular flow.

The advantages of this time-scale separation are twofold. Firstly, it simplifies (isolates) the simulation of acoustic propagation through a "frozen" (or a snapshot of) granular network at a given flowing instance. Here the interparticle friction coefficients may be modified solely by the irreversible ultrasound-matter interaction (Johnson & Jia 2005; Jia *et al.* 2011; Leópoldès *et al.* 2020) and are not affected by particle collisions or other phenomena occurring at the *grain-motion time scale*. Additionally, this approach offers high computational efficiency since we can use relatively large time steps ($\Delta t_g = 1\,\text{ms}$ at the *grain-motion time scale*) without losing the ultrasound-induced effects, thereby allowing for the consideration of large assemblies of grains that can be compared to experimental data in laboratory settings (see typical times of simulations in Martin *et al.* (2023*a*)). The computational time efficiency is discussed in Section 2.4. The model utilized at the grain motion time scale is the convex optimization contact dynamics (COCD) discrete element method, which has been proposed and validated in Martin *et al.* (2023*a*), and compared with other granular models in Martin *et al.* (2023*b*).

The numerical method is presented at various time scales in Section 2. Section 3 contains all the results we obtain, both with and without destabilization due to basal vibrations. In Section 4, we then discuss the physical interparticle mechanisms responsible for the destabilization we have identified, the changes that occur when we alter the vibration parameters, and compare our results with experiments.

2. Numerical models for granular flows and ultrasonic vibrations

To model the acoustic triggering of granular flows induced by basal ultrasounds at the laboratory scale, our strategy is to take into account the vibration-induced change of the interparticle friction coefficient μ_p. This is done by considering the very different time scales of grain motion and ultrasounds, respectively. We then consider a *grain-motion time scale* that is of the order of small grain motions, and a *vibration time scale*.

Concerning the *grain-motion time scale*, for a granular flow on a slope, the horizontal velocity scale is given by $U = \sqrt{gH\cos\theta}$, where g is the gravitational constant, H is the thickness of the granular mass, and θ is the slope angle. In our configuration, H lies between $3d$ and $14.4d$, where d is the mean diameter of the grains (0.7 mm), resulting in $0.002 \leqslant H \leqslant 0.011\,\text{m}$, and thus $0.14 \lesssim U \lesssim 0.32\,\text{m}\,\text{s}^{-1}$. We use a time scale where a grain moving at velocity U covers its own radius, i.e., $L = 0.35\,\text{mm}$. This time scale is then given by $T = L/U$, and it falls within the range of approximately $10^{-3} \lesssim T \lesssim 2.5 \times 10^{-3}\,\text{s}$. We adopt the smallest value as the common time scale for all our grain displacement simulations, i.e., the *grain-motion time scale* is $\Delta t_g = 1\,\text{ms}$.

Regarding the *vibration time scale*, experimental measurements of the speed of sound in a granular assembly at rest and maintained by a low confined stress (for instance by gravity) have been made where small but finite values of sound speed $c = 10\,\text{m}\,\text{s}^{-1}$ to $100\,\text{m}\,\text{s}^{-1}$ were measured (Liu & Nagel 1992; Bonneau *et al.* 2008; van den Wildenberg *et al.* 2013; Brum *et al.* 2019). These values are much larger than the sound speed predicted by the

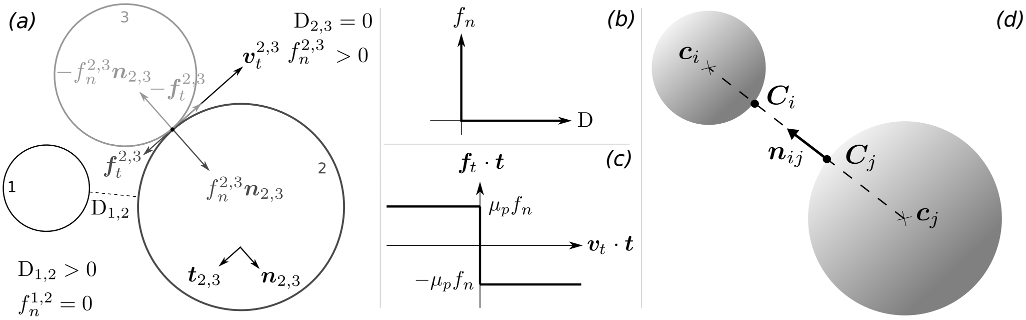

Figure 2: 2D schematic depiction of the two contact laws. *(a)* Representation of a three-disk situation: Disks 1 and 2 are not in contact, while disks 2 and 3 are. D_{ij}, $(1 \leqslant i < j \leqslant 3)$ indicates the normal distance between disks i and j, f_n^{ij} is the normal force's intensity at the contact, $\boldsymbol{n}_{2,3}$ (resp. $\boldsymbol{t}_{2,3}$) is the unit normal (resp. tangential) vector at the contact between 2 and 3, $\boldsymbol{f_t}^{2,3}$ denotes the tangential force vector, and $\boldsymbol{v_t}^{2,3}$ is the tangential relative velocity vector between disks 2 and 3. *(b)* Graph representing the normal law. *(c)* Graph depicting the Coulomb friction law. $\boldsymbol{x} \cdot \boldsymbol{y}$ denotes the dot product of vectors $\boldsymbol{x}$ and $\boldsymbol{y}$. *(d)* Notations in 3D.

effective medium theory based on the simplified normal contact force (i.e., the Hertz model), $c \simeq p^{1/6}$ in a granular pack loaded by a hydrostatic pressure $p = \rho g h$. This would give rise to $c \simeq 0.1\,\mathrm{m\,s^{-1}}$ for $h = 5\,\mathrm{mm}$ to $10\,\mathrm{mm}$. Such a discrepancy may stem from the interlocking effect (i.e., arching) due to frictional contact (tangential) forces and heterogeneous anisotropic stress networks (i.e., force-chains), which depend on the sample configuration and loading history (memory effect) as well as the confining boundary (Jaeger *et al.* 1990). As shown in Khidas & Jia (2010) and Johnson *et al.* (1998), elastic wave velocities (longitudinal and transversal) do remain finite in a compacted granular packing after the removal of the applied stress, likely due to the tight wedging or interlocking of grains which results in a residual stress network. Using again the mean grain radius as a characteristic distance, we get a time scale approximately from $T = L/c$, i.e., $T \simeq 12\,\mathrm{\mu s}$, estimated with $c = 30\,\mathrm{m\,s^{-1}}$ (Leópoldès *et al.* 2020). Hence, we adopt this value as the time scale for sound propagation $\Delta t_w = 10\,\mathrm{\mu s}$. Note that it is smaller than the grain displacement time scale by a factor of 100, justifying our approach that separates these two time scales.

Consequently, at the *vibration time scale* Δt_w, the granular assembly can be considered as frozen. We thus consider two different models at these two different time scales. At the *grain-motion time scale* Δt_g, grain motion is described based on the discrete element method COCD (Martin *et al.* 2023*a*), which represents the macroscopic motion of each particle in a granular assembly. Then, at the *vibration time scale*, the *vibration model* computes the infinitesimal perturbations of each grain position, around an equilibrium configuration provided by the *grain-motion model*. We first briefly introduce the *grain-motion model* COCD developed by Martin *et al.* (2023*a*) (Section 2.1). Then we present the the *wave equation* and the *vibration model* (Section 2.2), and finally describe the *Mindlin model* (Section 2.3) that deals with the vibration-induced reduction of interparticle friction coefficients. We close this modeling section by briefly presenting the computational time efficiency (Section 2.4).

2.1. *Grain-motion model* COCD

In our *grain-motion model* COCD, the granular media is represented by a collection of rigid particles (see Fig. 1(a)) like glass spheres (Martin *et al.* 2023*a*). The equations of motion are solved for each particle at every time step to determine their respective contact forces. These interactions are traditionally described using the Hertz theory, utilizing non-linear damped springs as commonly seen in the molecular dynamics (MD) framework (see Cundall's pioneering work in Cundall & Strack (1979)). However, in this article, we adopt an alternative method called contact dynamics (CD), originally introduced by Moreau and Jean in the 1990s (Moreau 1988; Jean & Moreau 1992; Moreau 1994, 1999; Jean 1999; Moreau 2004). In contrast to MD, where contact forces are modeled using functions derived from the Hertz theory, CD employs linear impulses. These impulses adhere to contact laws governing both normal repulsion and tangential friction.

Numerous numerical techniques have been put forth for CD models (Maury 2006; Staron & Hinch 2005; Anitescu 2006; Tasora *et al.* 2008; Radjai & Richefeu 2009; Acary *et al.* 2011; Seguin *et al.* 2016; Martin *et al.* 2023*a*; Bloch & Lefebvre-Lepot 2023). Close to the framework of the SCoPI software (2022), in COCD's approach, particle velocities and positions are computed simultaneously through an implicit scheme, necessitating the solution of a convex minimization problem during each time integration step.

Within the CD framework, two contact laws are validated at each contact and time step. The first law establishes a complementarity problem between the normal distance and the intensity of the normal contact force. This implies that grains cannot overlap or engage in interaction unless they are in contact, and the force between any two grains is inherently repulsive. In mathematical terms, this relationship is represented as

$$f_n^{ij} \geqslant 0\,,\;\; \mathrm{D}_{ij} \geqslant 0\,,\;\; f_n^{ij}\mathrm{D}_{ij} = 0,$$

where i and j denote two particles, D_{ij} is their normal distance, and f_n^{ij} represents the intensity of the normal force between them (see Fig. 2(a) and Fig. 2(b)). The second validated contact law pertains to Coulomb friction law (Fig. 2(a) and Fig. 2(c)), encompassing both the tangential and normal components of the contact force belonging to Coulomb's cone, is expressed as

$$\begin{aligned} \boldsymbol{f}_t^{ij} &= -\mu_{ij} f_n^{ij}\, \boldsymbol{v}_t^{ij}/\|\boldsymbol{v}_t^{ij}\|, && \text{if} \quad \|\boldsymbol{v}_t^{ij}\| > 0, \\ \|\boldsymbol{f}_t^{ij}\| &\leqslant \mu_{ij} f_n^{ij}, && \text{if} \quad \|\boldsymbol{v}_t^{ij}\| = 0, \end{aligned}$$

where $\|\cdot\|$ denotes the euclidean norm, μ_{ij} is the interparticle friction coefficient (μ_p), $\boldsymbol{f}_t^{ij} \in \mathbb{R}^3$ denotes the tangential force vector, and $\boldsymbol{v}_t^{ij} \in \mathbb{R}^3$ is the tangential relative velocity vector between the two spheres i and j. To be as general as possible, we will subsequently introduce the equations of motion in 3D despite the simulations that are presented in this article are in 2D.

Consider a mechanical system in $\mathbb{R}^3$, consisting of N rigid spheres capable of rotation, each with specified fixed radii $r_i > 0$ and masses $m_i > 0$, $i = 1, \ldots, N$. The center of sphere i is represented by $\boldsymbol{c}_i \in \mathbb{R}^3$, and its instantaneous velocity by $\boldsymbol{v}_i \in \mathbb{R}^3$. As we are exclusively dealing with spheres, we do not track the orientation of bodies; instead, we focus solely on the instantaneous rotation vector, denoted as $\boldsymbol{\omega}_i \in \mathbb{R}^3$. We denote by

$$\boldsymbol{c} = (\boldsymbol{c}_1, \ldots, \boldsymbol{c}_N) \in \mathbb{R}^{3N} \text{ and } \boldsymbol{u} = (\boldsymbol{v}_1, \boldsymbol{\omega}_1, \ldots, \boldsymbol{v}_N, \boldsymbol{\omega}_N) \in \mathbb{R}^{6N}$$

the generalized position and velocity field vectors.

The signed distance between spheres i and j is defined by :

$$\mathrm{D}_{ij}(\boldsymbol{c}) = \|\boldsymbol{c}_i - \boldsymbol{c}_j\| - \left(r_i + r_j\right), \tag{2.1}$$

so that the non-overlapping condition writes $\mathrm{D}_{ij} \geqslant 0$.

For any pair of grains i and j, with respective centers represented by $\boldsymbol{c}_i$ and $\boldsymbol{c}_j$, we use $\boldsymbol{C}_i$ and $\boldsymbol{C}_j$ to indicate the points that establish the distance (with $\boldsymbol{C}_i = \boldsymbol{C}_j$ when the spheres are in contact; refer to Fig. 2(d)). We define the corresponding position vectors as $\boldsymbol{r}_i = \boldsymbol{C}_i - \boldsymbol{c}_i$, $\boldsymbol{r}_j = \boldsymbol{C}_j - \boldsymbol{c}_j$.

We define the direction perpendicular to the surfaces of the particles at points $\boldsymbol{C}_i$ and $\boldsymbol{C}_j$, a direction common to both particles. We introduce the unit vector $\boldsymbol{n}_{ij} \in \mathbb{R}^3$, which is defined as the corresponding normal vector pointing towards particle i. Given that we are dealing with spherical particles, we have:

$$\boldsymbol{n}_{ij} = \frac{\boldsymbol{c}_i - \boldsymbol{c}_j}{\|\boldsymbol{c}_i - \boldsymbol{c}_j\|}.$$

We denote by $\boldsymbol{P}_{ij}\boldsymbol{v} = \boldsymbol{v} - (\boldsymbol{v} \cdot \boldsymbol{n}_{ij})\boldsymbol{n}_{ij} \in \mathbb{R}^3$ the projection of $\boldsymbol{v}$ on Π_{ij}, the plane that is orthogonal to $\boldsymbol{n}_{ij}$ and thus parallel to the tangent planes in $\boldsymbol{C}_i$ and $\boldsymbol{C}_j$.

We also define $\boldsymbol{A}_{ij}$ from $\mathbb{R}^{6N}$ to $\mathbb{R}^3$ as the linear operator which maps the generalized velocity field $\boldsymbol{u} \in \mathbb{R}^{6N}$ to the relative velocity between the points $\boldsymbol{C}_i$ and $\boldsymbol{C}_j$ at which the distance between spheres i and j is attained, i.e.

$$\boldsymbol{A}_{ij}\boldsymbol{u} = \boldsymbol{v}_i + \boldsymbol{\omega}_i \wedge \boldsymbol{r}_i - (\boldsymbol{v}_j + \boldsymbol{\omega}_j \wedge \boldsymbol{r}_j) \in \mathbb{R}^3.$$

Direct calculations demonstrate that for any generalized velocity $\boldsymbol{u} \in \mathbb{R}^{6N}$ and any vector $\boldsymbol{f} \in \mathbb{R}^3$, we obtain $\boldsymbol{A}_{ij}\boldsymbol{u} \cdot \boldsymbol{f} = \boldsymbol{u} \cdot \boldsymbol{A}_{ij}^T\boldsymbol{f}$ with

$$\boldsymbol{A}_{ij}^T\boldsymbol{f} = (\boldsymbol{0}, \dots, \boldsymbol{0}, \underbrace{\boldsymbol{f}, \boldsymbol{r}_i \wedge \boldsymbol{f}}_{\text{position } i}, \boldsymbol{0}, \dots, \boldsymbol{0}, \underbrace{-\boldsymbol{f}, -\boldsymbol{r}_j \wedge \boldsymbol{f}}_{\text{position } j}, \boldsymbol{0}, \dots, \boldsymbol{0}) \in \mathbb{R}^{6N},$$

so that $\boldsymbol{A}_{ij}^T$ maps a vector $\boldsymbol{f} \in \mathbb{R}^3$ to the generalized force/moment vector corresponding to the force $\boldsymbol{f}$ exerted on particle i at point $\boldsymbol{C}_i$ and the opposite force $-\boldsymbol{f}$ exerted on particle j at point $\boldsymbol{C}_j$.

The vector $\boldsymbol{P}_{ij}\boldsymbol{A}_{ij}\boldsymbol{u} = \boldsymbol{v}_t^{ij} \in \mathbb{R}^3$ represents the tangential relative velocity. Consequently, when two spheres are in contact without any relative normal motion (i.e., $\boldsymbol{n}_{ij} \cdot \boldsymbol{A}_{ij}\boldsymbol{u} = 0$), the expression $\|\boldsymbol{P}_{ij}\boldsymbol{A}_{ij}\boldsymbol{u}\| = 0$ indicates a rolling motion with no slip, while $\|\boldsymbol{P}_{ij}\boldsymbol{A}_{ij}\boldsymbol{u}\| > 0$ corresponds to a sliding motion.

At any time, we shall denote by I_c the set of all possible pairs of contacts: $I_c = \{(i, j)\ 1 \leqslant i < j \leqslant N\}$. Note that the pair of grains i and j is represented only once in I_c through the couple (i, j) if $i < j$ and (j, i) if $j < i$. We denote by N_c the total number of potential pairs of spheres, which is also the cardinal of set I_c, i.e., $N_c = \text{card}(I_c) = N(N-1)/2$.

We consider that no external torque is exerted on the grains. If $\boldsymbol{f}_i^{ext} \in \mathbb{R}^3$ is the external force exerted on particle i, we define the generalized force vector as $\boldsymbol{f}^{ext} = (\boldsymbol{f}_1^{ext}, 0, \dots, \boldsymbol{f}_n^{ext}, 0) \in \mathbb{R}^{6N}$. We then define the $6N \times 6N$ generalized mass matrix (masses and moments of inertia) as

$$\boldsymbol{M} = \text{diag}\,(m_1, m_1, m_1, J_1, J_1, J_1, m_2, \dots, J_N, J_N, J_N)\,.$$

Finally, the equations of motion write:

$$\boldsymbol{M}\frac{\mathrm{d}\boldsymbol{u}}{\mathrm{d}t} = \boldsymbol{f}^{ext} + \sum_{\alpha \in I_c} \boldsymbol{A}_\alpha^T \left(f_n^\alpha \boldsymbol{n}_\alpha + \boldsymbol{f}_t^\alpha\right), \tag{2.2}$$

$$f_n^\alpha \geqslant 0\,,\ \mathrm{D}_\alpha \geqslant 0\,,\ f_n^\alpha \mathrm{D}_\alpha = 0, \quad \alpha \in I_c, \tag{2.3}$$

$$\text{If } \mathrm{D}_\alpha(\boldsymbol{c}) = 0 \text{ then } (\boldsymbol{A}_\alpha \boldsymbol{u}^+) \cdot \boldsymbol{n}_\alpha = 0, \quad \alpha \in I_c, \tag{2.4}$$

$$\text{If } \|\boldsymbol{P}_\alpha \boldsymbol{A}_\alpha \boldsymbol{u}^+\| > 0 \text{ (sliding motion)}\,,\ \boldsymbol{f}_t^\alpha = -\mu_\alpha f_n^\alpha \frac{\boldsymbol{P}_\alpha \boldsymbol{A}_\alpha \boldsymbol{u}^+}{\|\boldsymbol{P}_\alpha \boldsymbol{A}_\alpha \boldsymbol{u}^+\|}, \quad \alpha \in I_c, \tag{2.5}$$

$$\text{If } \|\boldsymbol{P}_\alpha \boldsymbol{A}_\alpha \boldsymbol{u}^+\| = 0 \text{ (no slip)}\,,\ \|\boldsymbol{f}_t^\alpha\| \leqslant \mu_\alpha f_n^\alpha, \quad \alpha \in I_c. \tag{2.6}$$

Equation (2.4) is added to the normal (Eq. (2.3)) and tangential contact laws (Eqs. (2.5)-

(2.6)), specifying an inelastic collision law. Observe that translational and rotational velocities are prone to being non-smooth, experiencing instantaneous jumps during collisions. Specifically, the post-collision velocity $\boldsymbol{u}^+$ may differ from the pre-collision velocity $\boldsymbol{u}^-$. Consequently, the mentioned evolution is to be interpreted in a weak, distributional sense.

Let's provide some additional remarks on the preceding equations. For a pair of grains $\alpha = (i, j) \in I_c$, where I_c denotes the set of contacts, the corresponding vector $f_n^{ij}\boldsymbol{n}_{ij} + \boldsymbol{f}_t^{ij} \in \mathbb{R}^3$ is transmitted to both particles i and j through the transpose of $\boldsymbol{A}_{ij}$. To elaborate, let's introduce the following definitions:

$$f_n^{ji} = f_n^{ij}, \quad \boldsymbol{f}_t^{ji} = -\boldsymbol{f}_t^{ij}, \quad \forall\alpha = (i, j) \in I_c.$$

Then, utilizing the expression for $\boldsymbol{A}_{ij}^T$, Eq. (2.2) can be reformulated as follows:

$$\begin{aligned} m_i\,\dot{\boldsymbol{v}}_i &= \boldsymbol{f}_i^{ext} + \sum_{j,j\neq i}(f_n^{ij}\boldsymbol{n}_{ij} + \boldsymbol{f}_t^{ij}), \quad \forall i = 1\ldots N,\\ J_i\,\dot{\boldsymbol{\omega}}_i &= \sum_{j,j\neq i}(\boldsymbol{r}_i \wedge \boldsymbol{f}_t^{ij}), \quad \forall i = 1\ldots N. \end{aligned}$$

This corresponds to Newton's second law, where the contact between particles i and j induces the force $f_n^{ij}\boldsymbol{n}_{ij} + \boldsymbol{f}_t^{ij}$ on particle i. The reciprocity of this contact's action on both particles is evident from the definitions of f_n^{ji} and $\boldsymbol{f}_t^{ji}$, derived from f_n^{ij} and $\boldsymbol{f}_t^{ij}$. The normal force exerted on sphere i due to this contact is $f_n^{ij}\boldsymbol{n}_{ij}$, and $\boldsymbol{f}_t^{ij} \in \Pi_{ij}$ represents the frictional (tangential) force, which lies in the plane orthogonal to $\boldsymbol{n}_{ij}$.

From Eq. (2.3), we deduce $f_n^{ij} = f_n^{\alpha} \geqslant 0$. This, combined with the orientation of $\boldsymbol{n}_{ij}$ from particle j to particle i, ensures that this force is repulsive, as anticipated. Equation (2.3) also guarantees that the distances between the particles remain positive, and the normal force is null whenever the distance is strictly positive (i.e., the particles are not in contact).

The mechanical characteristics of such granular media arise from a synergy of geometrical particle rearrangements and interparticle friction forces. To be precise, the macroscopic static friction coefficient $\mu_s = \tan(\theta_m)$ — with θ_m the (maximum) angle of avalanche — can be understood as a composite of the interparticle friction coefficient μ_p and the geometric confinement effect (dilatancy) μ_g (Leópoldès *et al.* 2020). The coefficient μ_g is influenced by factors such as grain shapes, masses, or inertia, while μ_p serves as a defined parameter within the model, integral to the classical Coulomb law of friction for all grain-to-grain or grain-to-wall interactions.

The value of μ_p employed in this article is $\mu_p = 0.25$. This choice falls within a comparable range to the friction coefficient $\mu_p = 0.3$, calibrated through 3D simulations and experiments (Martin *et al.* 2023*a*,*b*), and the friction coefficient measured for an ideal glass-to-glass contact, $\mu_p = 0.4$ (www.engineeringtoolbox.com 2022), as well as that determined using DEM, $\mu_p = 0.16$ (Tang *et al.* 2019).

2.2. *Wave equation and vibrational modes*

2.2.1. *Wave equation*

At the wave propagation or *vibration time scale*, the grains motions may be supposed quasi-static or frozen. As mentioned above, however, the quantitative description of sound propagation in such weakly confined amorphous-like granular media is not available (Makse *et al.* 2004). To capture qualitatively the interaction between and ultrasound granular flow (see Section 2.3), we model the vibration of grains, for a first approximation, as in a 2D network of mass-spring (mimicking a normal contact stiffness). Here the tangential force and rotational motion are neglected , i.e., the particles are considered as frictionless. Nevertheless, the friction forces are accounted for in the *grain-motion model* cocd and for investigating the lubrication effect at grain contacts induced by shear acoustic waves (see below section 2.3). The sound propagation is characterized by the perturbed positions of the centers of the masses $\boldsymbol{c}_i \in \mathbb{R}^3$; see .e.g., a similar model proposed in Somfai *et al.* (2005). Thanks to an expansion around an assumed equilibrium configuration, we establish a *wave equation* for infinitesimal perturbations from this equilibrium position. The full description of the equations derivation can be found in Appendix A.

Similarly to the operator $\boldsymbol{P}_{ij}\boldsymbol{A}_{ij}$ and since we do not account for rotational motion, we define $\boldsymbol{N}_{ij}$ as the linear operator from $\mathbb{R}^{3N}$ to $\mathbb{R}$ which maps the generalized grain velocity vector of translation $\bar{\boldsymbol{u}} = (\boldsymbol{v}_1, \boldsymbol{v}_2, \ldots, \boldsymbol{v}_N) \in \mathbb{R}^{3N}$ to the relative normal velocity between the spheres i and j (grains), projected on the line generated by the normal vector $\boldsymbol{n}_{ij}$, i.e.,

$$\boldsymbol{N}_{ij}\bar{\boldsymbol{u}} = (\boldsymbol{v}_i - \boldsymbol{v}_j) \cdot \boldsymbol{n}_{ij} \in \mathbb{R}.$$

Straightforward computations show that for any generalized velocity $\bar{\boldsymbol{u}} \in \mathbb{R}^{3N}$ and any scalar $f_n \in \mathbb{R}$, we have $f_n \boldsymbol{N}_{ij}\bar{\boldsymbol{u}} = \bar{\boldsymbol{u}} \cdot \boldsymbol{N}_{ij}^T f_n$ with

$$\boldsymbol{N}_{ij}^T f_n = (\boldsymbol{0}, \ldots, \boldsymbol{0}, \underbrace{f_n \boldsymbol{n}_{ij}}_{\text{position } i}, \boldsymbol{0}, \ldots, \boldsymbol{0}, \underbrace{-f_n \boldsymbol{n}_{ij}}_{\text{position } j}, \boldsymbol{0}, \ldots, \boldsymbol{0}) \in \mathbb{R}^{3N}, \tag{2.7}$$

so that $\boldsymbol{N}_{ij}^T$ maps a scalar $f_n \in \mathbb{R}$ to the generalized force vector corresponding to the force $f_n \boldsymbol{n}_{ij}$ exerted on particle i at point $\boldsymbol{c}_i$ and the opposite force $-f_n \boldsymbol{n}_{ij}$ exerted on particle j at point $\boldsymbol{c}_j$.

We then define the linear operator $\boldsymbol{N}$ from $\mathbb{R}^{3N}$ into $\mathbb{R}^{N_c}$ corresponding to the combination of all maps $\boldsymbol{N}_\alpha$, $\alpha \in I_c$, i.e., for any $\boldsymbol{v} \in \mathbb{R}^{3N}$, we have $\boldsymbol{N}\boldsymbol{v} = (\boldsymbol{N}_{1,2}\boldsymbol{v}, \boldsymbol{N}_{1,3}\boldsymbol{v}, \ldots, \boldsymbol{N}_{N-1,N}\boldsymbol{v}) \in \mathbb{R}^{N_c}$, and for any $\boldsymbol{f} \in \mathbb{R}^{N_c}$ we have the equality $\boldsymbol{N}\boldsymbol{v} \cdot \boldsymbol{f} = \boldsymbol{v} \cdot \boldsymbol{N}^T \boldsymbol{f}$.

We now define the $N_c \times N_c$ diagonal square matrix $\boldsymbol{K}$, which contains the elastic properties of the system by

$$\begin{aligned}\boldsymbol{K} = \frac{3}{2}\operatorname{diag}\Big((\kappa_{1,2})^{2/3}(f_n^{1,2})^{1/3}, \ldots \\ \ldots, (\kappa_{ij})^{2/3}(f_n^{ij})^{1/3}, \ldots \\ \ldots, (\kappa_{N-1,N})^{2/3}(f_n^{N-1,N})^{1/3}\Big) \in \mathbb{R}^{N_c \times N_c},\end{aligned}$$

where f_n^{ij} still represents the intensity of the normal force between particles i and j and where $\kappa_{ij} > 0$ is a constant depending on grains properties; see Appendix A.1.

We finally define the $3N \times 3N$ generalized mass matrix (masses only) as

$$\bar{\boldsymbol{M}} = \operatorname{diag}\left(m_1, m_1, m_1, m_2, m_2, m_2 \ldots, m_N, m_N, m_N\right). \tag{2.8}$$

At the end, a *wave equation* is defined for any $\boldsymbol{e} \in \mathbb{R}^{3N}$ by

$$\bar{\boldsymbol{M}}\frac{\mathrm{d}^2\boldsymbol{e}}{\mathrm{d}t^2} + \boldsymbol{\Lambda}\boldsymbol{e} = 0, \tag{2.9}$$

where the linear map defined by the matrix

$$\boldsymbol{\Lambda} = \boldsymbol{N}^T\boldsymbol{K}\boldsymbol{N} \in \mathbb{R}^{3N \times 3N},$$

can be seen as a kind of discrete Laplace operator, and where ε indicates that $\boldsymbol{e}$ is only an infinitesimal perturbation of configuration $\boldsymbol{c}$.

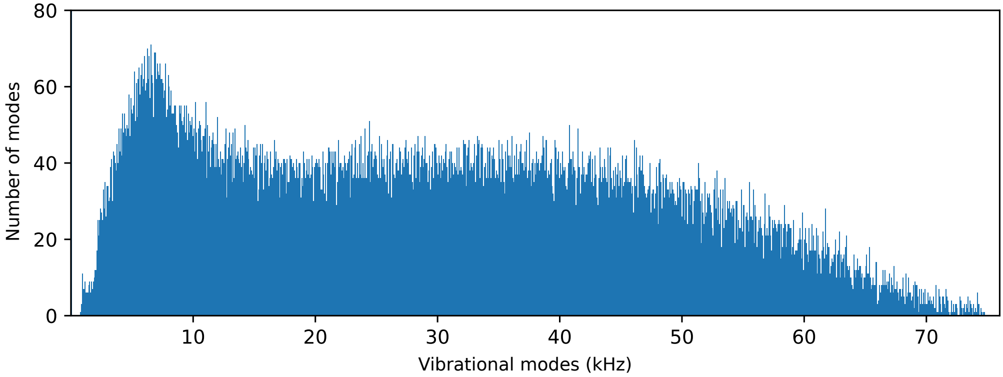

Figure 3: Histogram of the *vibrational (i.e., eigen) modes* of the quasi-static system considered at the *vibration time scale*, computed for a plane slope $\theta = 14°$, flow height $H/d = 14.4$ at $t = 1.2$ s. There are about 32 000 modes presented in this figure.

The operator $\boldsymbol{\Lambda}$ depends on the contact network through operator $\boldsymbol{N}$, formed by the generalized position vector at equilibrium $\boldsymbol{c}$ and embeds the elastic properties of the granular assembly, characterized by the constant normal force intensities exerted between any particles i and j, i.e., $f_n^{ij} \geqslant 0$ for $1 \leqslant i < j \leqslant n$. These normal force intensities f_n^{ij} are provided by the *grain-motion model* resolving the normal, tangential, and collision laws (see Section 2.1 and Refs. Maury (2006); Martin *et al.* (2023*a*)) and they are not modified by the vibrations at the *vibration time scale*.

In the classical form of the wave equation ($\partial_t^2 u - c^2 \Delta u = 0$), the square of the sound speed (constant) c^2 is before the Laplace operator Δ. In our framework Eq. (2.9), the (local) sound speeds are then proportional to $((\kappa_{ij})^{2/3}(f_n^{ij})^{1/3}/m_i)^{1/2}$ so to the 1/6th power of the normal forces computed at the *grain-motion time scale* f_n^{ij}, i.e., $c \propto (f_n^{ij})^{1/6}$ (see discussions above and in Appendix A.1) .

2.2.2. *Vibration model*

We now present the *vibration model* which describes the asymptotic limit of the ultrasound vibrations (perturbations) induced in a quasi-static (frozen) granular packing. The generalized position vector of a grain at equilibrium, denoted $\boldsymbol{c} \in \mathbb{R}^{3N}$ is excited at a mono-frequency by an external vibration applied from the basal plane. More precisely, the grains in contact with the bottom are submitted to a sinusoidal motion, at a given frequency $f = \omega/2\pi$ and amplitude U_0.

At this *vibration time scale*, we seek for the *vibrational (eigen) modes* of the granular assembly, on the line of Leibig (1994) and Somfai *et al.* (2005), and consider the asymptotic limit regime (i.e., steady harmonic vibrations) of the perturbed positions of all grains at the forced external vibration frequency f. Accordingly, the solution to the *wave equation* (2.9) $\boldsymbol{e} \in \mathbb{R}^{3N}$ is *separable*, and can be written as $\boldsymbol{e}(t) = U_0 \exp(i\omega t)\boldsymbol{q}$, where $\boldsymbol{q} \in \mathbb{R}^{3N}$ is a constant vector that does not depend on time, solution to the *vibration model* (or Helmoltz equation (Somfai *et al.* 2005; Couto 2013)). This equation writes

$$\left(\omega^2 \mathbf{1}_{3N} + \boldsymbol{\Lambda}\right) \boldsymbol{q} = \mathbf{0} \in \mathbb{R}^{3N}, \tag{2.10}$$

associated to the Dirichlet kind of boundary condition

$$q_{i_y} = 1, \quad \forall i \in \mathcal{J}, \tag{2.11}$$

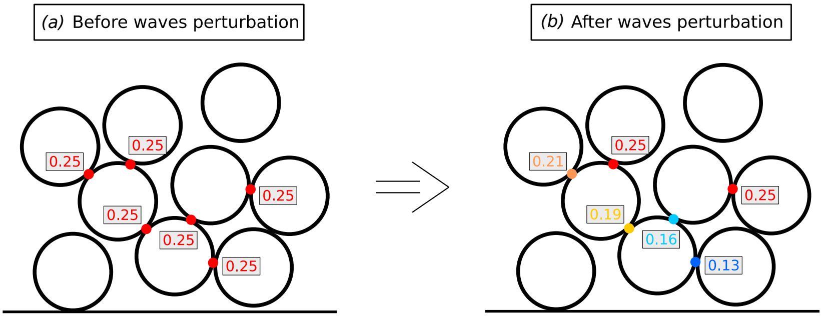

Figure 4: Illustration of the vibration-induced perturbations of the interparticle friction coefficients.

where $\mathcal{J} \subset \mathbb{N}$ is the set of grain indexes in contact with the bottom, $q_{i_y} \in \mathbb{R}$ is the vertical component of the vector $\boldsymbol{q}$, and $\mathbf{1}_{3N}$ is the $3N \times 3N$ identity matrix. Note that since the basal boundary condition is set only on spheres vertical component, the particles belonging to $\mathcal{J}$ are free to move on the horizontal plane.

The square matrix $\boldsymbol{\Lambda}$ is positive semi-definite and the *vibrational (eigen) modes* of the entire granular mass are directly given by its eigenvalues. Consequently, Eq. (2.10) is ill-posed when ω^2 is one of its eigenvalues generating eventually resonance effects. Nevertheless, except in these situations, one has the existence and the uniqueness of the solution given by $\boldsymbol{e}$. Figure 3 shows the histogram of the system normal (eigen) modes computed for a plane slope $\theta = 14°$ and a layer height $H/d = 14.4$ at $t = 1.2$ s of simulated flow time—a typical set of parameters used for our simulations presented in Section 3.

Note that to mimic the sound speed $c \simeq 10\,\mathrm{m\,s^{-1}}$ (and associated effective contact stiffness) observed in the experiments mentioned above, we have adjusted empirically the contact coefficients κ_{ij} (as a kind of fit parameter) in our simplified Hertz model (see Appendix A.1).

2.3. *Interparticle friction reduction through acoustic lubrication*

Let us outline here the coupling between the *grain-motion model* COCD (see Section 2.1) and the *vibration model* (Eqs. (2.10)-(2.11)), and the role played by the acoustic lubrication given by the *Mindlin model*. More precisely, the purpose of the *vibration model* associated to the *Mindlin model* is to compute a new coefficient of friction for each contact, which embedded the vibrational perturbations into the dynamics that occurs at the *grain-motion time scale*. We consider that we are in the framework described in Section 2.2.2, where a mono-frequency sinusoidal vibration is imposed on the basal grains of a pile. In the following, we consider a temporal discretization of the *grain-motion model*; refer to Martin *et al.* (2023*a*) for the full description of the numerical scheme that is used for computing a numerical solution to COCD.

The coupling algorithm that we present in this article consists in running one iteration of the numerical scheme used to compute the solution of the *grain-motion model* with a typical time step $\Delta t_g = 1$ ms, providing the current generalized position vector $\boldsymbol{c} \in \mathbb{R}^{3N}$ and a set of the normal force intensities f_n^{ij}, $1 \leqslant i < j \leqslant N$. We then compute the solution $\boldsymbol{q} \in \mathbb{R}^{3N}$ to the *vibration model*. From the basal frequency f and infinitesimal amplitudes U_0, the *Mindlin model* gives us new values of the interparticle friction coefficients μ_{ij} that are used in the Coulomb's law of the next iteration of the *grain-motion model*; see Eqs. (2.5)-(2.6). In the following, we describe more precisely the way the friction coefficients are modified.

When the *vibration model* is solved, the vector $U_0\boldsymbol{q} \in \mathbb{R}^{3N}$ corresponds to the ultrasound-induced perturbations applied on the generalized position vector $\boldsymbol{c} \in \mathbb{R}^{3N}$ at each contact

H/d	N	t^0_{int}	t^{70}_{int}	$(t^{70}_{int} - t^0_{int})/t^{70}_{int}$
3	8000	1.24 s	2.44 s	49 %
6	13 319	2.32 s	4.03 s	42 %
8.7	20 142	5.21 s	7.91 s	34 %
11.4	24 000	10.29 s	14.46 s	29 %
14.4	32 000	13.04 s	17.50 s	26 %

Table 1: Statistics on computational time. H/d gives the normalized thickness of the granular layer, N is the number of grains, t^0_{int} and t^{70}_{int} are the average computational times required to complete one time integration—a simulated time of Δt_g—without ($f = 0\,$kHz) and with vibrations ($f = 70\,$kHz). The last column is the computational time (in percentage) spent for the calculation of vibrations and the reduction of the interparticle friction coefficients during one time integration. The MOSEK's tolerance parameter is set at the default value (10^{-8}, see details in Martin *et al.* (2023*a*)). The simulations were performed on one Intel® Core™ i7-1065G7 CPU @ 1.30 GHz × 8.

for the basal amplitude U_0 and frequency f. From there, the normal (respectively tangential) infinitesimal displacements at contact is given by $U_0\boldsymbol{N}_{ij}\boldsymbol{q} \in \mathbb{R}^{3N}$ (respectively $U_0\boldsymbol{P}_{ij}\boldsymbol{q} \in \mathbb{R}^{3N}$ with $\boldsymbol{P}_{ij}$ introduced in Section 2.1). The question now arises of how to account for the infinitesimal perturbations of grains onto their macroscopic motion. The observations made in Leópoldès *et al.* (2020) show that the ultrasounds lead to modifying the static friction coefficient at the contact. That is why we choose to model the feedback of the acoustic waves on grains motion through the modification of the interparticle friction coefficient μ_p, which is involved only in the tangential contact law (μ_{ij} in Coulomb's law) at the *grain-motion time scale*. Without the vibrations, we consider for the sake of simplicity that there is the same static friction coefficient for every contact but having different values of μ_p does not change the method.

More precisely, the static friction coefficient μ_s includes both the interparticle friction μ_p and the geometric trapping μ_g (dilatancy effect). Because of the small amplitude of ultrasound, we assume that the sound-matter interaction only modifies μ_p but not μ_g, hence the new vibration-induced static friction coefficient $\mu^\star_s$ is resulting from the modification of $\mu^\star_p \neq \mu_p$, only. It means that due to ultrasound propagation, the static friction coefficient μ_{ij} changes depending on perturbation amplitudes between grains. We then denote the vibration-induced interparticle static friction coefficient $\mu^\star_{ij}$. From the *Mindlin model* (see Léopoldès *et al.* (2013)), we consider that the decrease rate of the interparticle friction coefficient $\Delta\mu^\star_p/\mu_p$ is approximately proportional to the ratio of the microscopic oscillating tangential force to the static normal force intensities times the coefficient of friction (this product being actually the bound of the tangential force $\boldsymbol{f}^{ij}_t$ (see Eqs. (2.5)-(2.6))), i.e., $\Delta\mu^\star_p/\mu_p \propto -\delta\mathrm{f}^{ij}_t/(\mu_p f^{ij}_n)$, where $\delta\mathrm{f}^{ij}_t$ is the microscopic oscillating tangential force intensities. Accordingly, we adopt here this scaling formula for the granular layer to describe the acoustic lubrication of the interparticle friction coefficient

$$\frac{\mu^\star_{ij}}{\mu_p} = 1 - C_\mu \frac{\delta\mathrm{f}^{ij}_t}{\mu_p f^{ij}_n}, \tag{2.12}$$

where $C_\mu \geqslant 0$.

The remaining task is then to compute an estimation of ultrasound-induced oscillating tangential force intensities $\delta\mathrm{f}^{ij}_t$. We approximate these intensities through a linear elastic law, meaning that they are computed thanks to the microscopic tangential grains displacements,

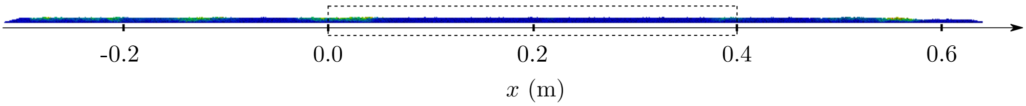

Figure 5: Full domain simulated. The dashed rectangle represent the observation domain of Figs. 6 and 9.

i.e., $\delta \mathrm{f}_t^{ij} = k_t^{ij} U_t^{ij}$, with k_t^{ij}, the shear contact stiffness and U_t^{ij}, the tangential displacement between the particles i and j given by $U_t^{ij} = U_0\|\boldsymbol{P}_{ij}\boldsymbol{q}\|$. Concerning the shear stiffness k_t^{ij}, we assume it verifies equation $k_t^{ij}/k_n^{ij} = 2/7$, which is a classical value used in discrete element models (DEMs) (Lemrich *et al.* 2017). Finally, the normal stiffness k_n^{ij} is given by the system elasticity embedded in matrix $\boldsymbol{\Lambda}$, i.e., $k_n^{ij} = (3/2)(\kappa_{ij})^{2/3}(f_n^{ij})^{1/3}$ (see Section 2.2.1). We can deduce the final form of $\mu_{ij}^\star$ as being $\mu_{ij}^\star/\mu_p = 1-(3U_0(\kappa_{ij})^{2/3})/(7\mu_p(f_n^{ij})^{2/3})\|\boldsymbol{P}_{ij}\boldsymbol{q}\|$. As a result, we then deduce a new set of interparticle friction coefficients which are provided to the *grain-motion model* before computing a new iteration (Fig. 4).

2.4. *Computational time efficiency*

At each time integration, the numerical scheme used to compute a numerical approximated solution to the *grain-motion model* requires solving a convex optimization problem. Additionally, the calculation of *vibrational (eigen) modes* and the modified friction coefficients are incorporated at each iteration. We utilize the MOSEK APS (2010) solver to address the optimization problem—see details in Martin *et al.* (2023*a*)—and for computing vibrational modes. Consequently, MOSEK is called twice an iteration. Note that thanks to our two-time scale approach, we do not need to reduce the time step of the numerical method (i.e., Δt_g) when integrating the influence of vibrations in our simulations. We maintain the same time step in cases with or without ultrasound. Computing the modes and new friction coefficients extends the total duration of each time integration. Table 1 provides some statistics on the computational times required for performing our simulations presented in Section 3. In particular, we observe that the proportion of time spent on modes and coefficients calculation decreases as the number of grains N increases (see the last column). For example, considering the vibrations increases the computation time of one iteration by 49 % for $N = 8000$ grains, whereas it only increases by 26 % for 32 000 grains. This result is promising because it shows that our method of time-scale separation allows us to account for the rheological modification of the flow by ultrasound with a reasonable additional computation time, especially as the number of grains is large.

3. Results

We now investigate the transition of the granular flow from the *jammed solid* state induced either by increasing shear or by basal ultrasound vibrations. The simulations presented in this section were all conducted in 2D, while we introduced the equations of the coupled model in 3D in Section 2. Therefore, the 2D static granular medium consists of layers of spherical grains (diameter d) of various mean thicknesses (from $H = 3d$ to $14.4d$) put on an inclined plane at a slope θ. The lengths of the samples are much larger than the thicknesses with free-stress boundary condition at both edges (Fig. 5). To observe the onset of grain motion, we focus on a specific observation domain, located at the middle of the full domain from 0.0 to 0.4 m (see the dashed rectangle in Fig. 5).

During a simulation, the slope of the basal plane is incrementally inclined (with a step $\Delta\theta = 0.5°$ between two consecutive slopes) for increasing the shear. At each new slope,

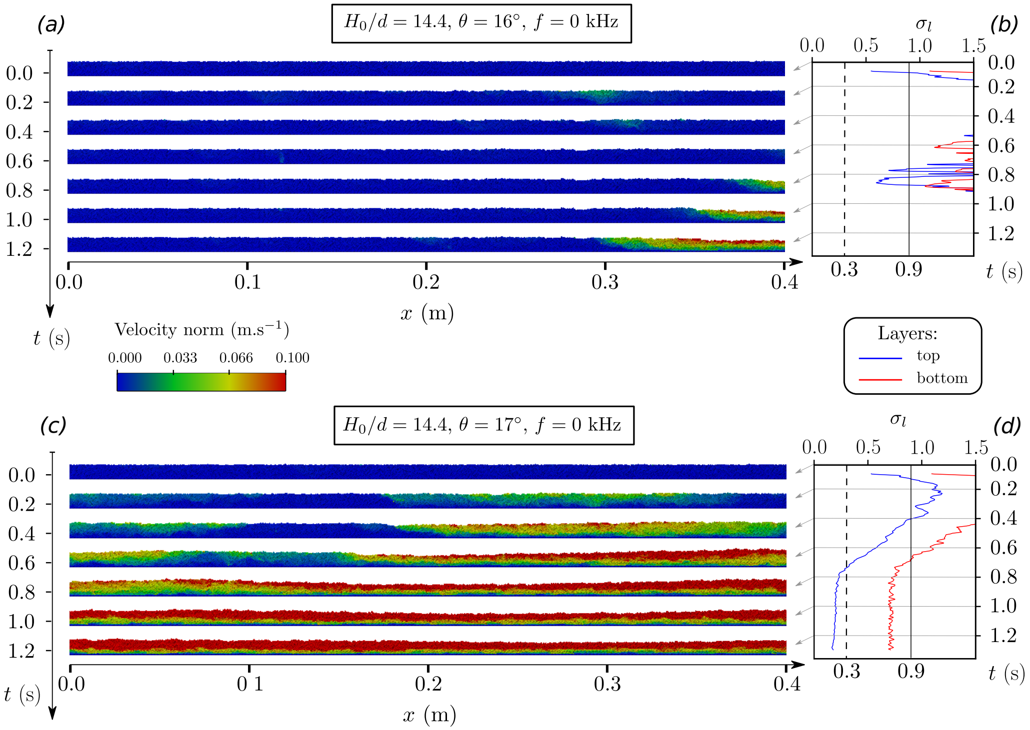

Figure 6: Granular assembly without basal vibrations ($f = 0$ kHz) at $\theta = 16°$ *(a, b)* and 17° *(c, d)* for $H = 14.4d$. *(a, c)* A sequence of 7 snapshots showing the evolution of a granular flow over time, ranging from $t = 0$ to 1.2 s. The color scale represents the magnitude of grain velocity. The observation domain covers a distance of 0.4 m and corresponds to the dashed rectangle in Fig. 5. *(b, d)* Variation, over the same time period, of the normalized standard deviation σ_l of grains' downslope velocity with respect to the average downslope velocity of the flow within two different layers decomposing the flow depth.

small amounts of grains may rearrange in the granular layer, increasing the kinetic energy E_k of the system and and the energy ratio E_k/E_t with E_t the total energy. The necessary condition to reach a new stable equilibrium (state) when the slope is increased from θ to $\theta + \Delta\theta$ is that this energy ratio satisfies the condition $E_k/E_t < \varepsilon_E$, during a simulated time of 0.1 s (equivalent to 100 iterations, since the *grain motion time step* is $\Delta t_g = 1$ ms). We used the value $\varepsilon_E = 3 \times 10^{-8}$, which has been empirically determined during pretests. When a portion of the mass detaches (and then $E_k/E_t \gg \varepsilon_E$), we check whether it is only a local rearrangement, e.g., as seen in Fig. 6(a) around $x = 0.3$ m at $t = 0.2$ s (which keeps moving slightly at 0.4 s but arrest flow at 0.6 s), or it leads to a generalized flow in space (Fig. 6(c)). In cases where the detachment (rearrangement) arrests on its own (i.e., $E_k/E_t < \varepsilon_E$ during 0.01 s), we continue the simulation by increasing the slope until there is a continuous flow. More specifically, in the case where grain motions triggered the ultrasound spread throughout the domain (E_k/E_t remains greater than ε_E), we simulate the flow for about 1.2 s without changing the slope.

During the simulated time, the flow depth is considered to be split into two layers of equal depth (index 1 refers to the top surface layer and index 2 to the bottom layer). For each layer, we compute the normalized standard deviation σ_l, with $l = 1, 2$ of grains' velocity relative

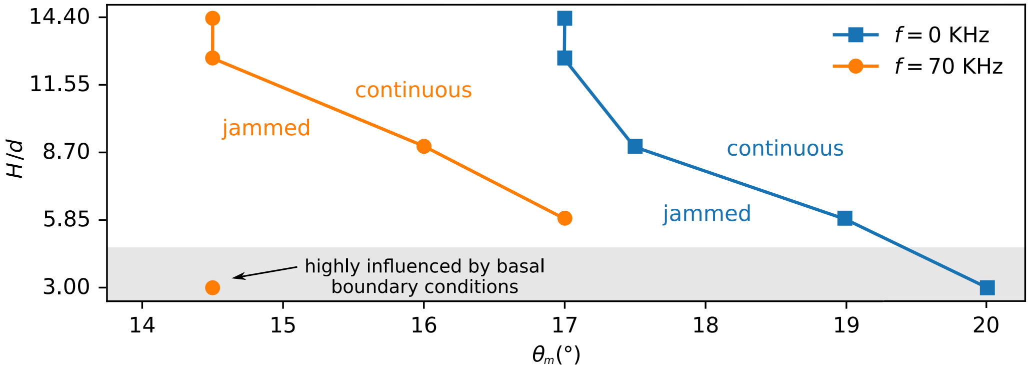

Figure 7: Phase space separating jammed and continuous regimes as a function of the avalanche angle θ_m and the flow thickness ratio H/d. Each point represents the avalanche angle for the five thickness ratios $H/d = 3$, 6, 8.7, 11.4, and 14.4. The blue curves represent these avalanche angles without basal vibrations ($f = 0$ kHz), contrary to the orange ones ($f = 70$ kHz).

to the average velocity (Figs. 6(b, d)), i.e.

$$\sigma_l = \frac{1}{\bar{v_{xl}}}\sqrt{\frac{1}{N_l}\sum_{i=1}^{N_l}(v_{ix} - \bar{v_{xl}})^2}, \tag{3.1}$$

where $N_l \in \mathbb{N}$ is the number of particles belonging to the layer l in the observation domain (Fig. 5), v_{ix} is the downslope velocity component of the disk i, and $\bar{v_{xl}}$ is the mean downslope velocity of the layer l, i.e., $\bar{v_{xl}} = (1/N_l)\sum_{i=1}^{N_l} v_{ix}$. If both σ_l values converge to a limit below than two specified criteria ε_{σ_l}, $l = 1, 2$ (determined empirically), the flow is considered as *uniform* (*continuous flow*) and we determine the angle as the avalanche angle and denote it by θ_m (see, e.g., Fig. 6(d) at $t = 0.8$ s). We then assume the steady regime of inertial flow is reached when the two σ_l are lower roughly than 0.3 for the top layer ($\varepsilon_{\sigma_1} = 0.3$, vertical dashed line) and 0.9 for the bottom layer ($\varepsilon_{\sigma_2} = 0.9$, vertical plain line). Once the avalanche angle θ_m is reached, other simulations are conducted for increasing angles larger than θ_m, up to 22°, starting each time from the final configuration of the largest angle where the layer remains static (i.e., $\theta_m - \Delta\theta$).

We start by considering the case where the flow is solely induced by gravity-driven shear, i.e., by the inclination of the plane (Section 3.1), that is, without any vibration of the basal plane. Secondly, we present the effect of triggering and the dynamics generated by the dual effect of the slope inclination and basal vibration (Section 3.2).

3.1. *Flow onset induced by gravity-driven shear: delay time to homogeneous flow*

Figures 6(a)-(d) depict grain motion in the zoomed regions for $H = 14.4d$, at inclination angles close below (16°) and equal to the avalanche angle θ_m (17°). When the inertial flow is initiated, a delay time is clearly observed before all grains are in motions (downslope flow) initiated from the low edge (on the right) (Figs. 6(a, c)). Comparing the grains' velocity norm at $\theta = 16°$ and 17° at $t = 1.2$ s, we observe that the moving part of the domain (the low edge in Fig. 6(a) and the full domain in Fig. 6(c)) is intuitively 40 % slower at 16° than at 17°. Additionally, Fig. 6(c) shows that in the first moments, the flow is initiated not only from the low edge but also in the middle of the domain; see, e.g., the motion started by the collection of particles centered in $x = 0.28$ m at 0.2 s and the motion initiated from the high edge (on the left) at 0.4 s (Fig. 6(c)). At 0.8 s, these two moving assembly of particles have merged

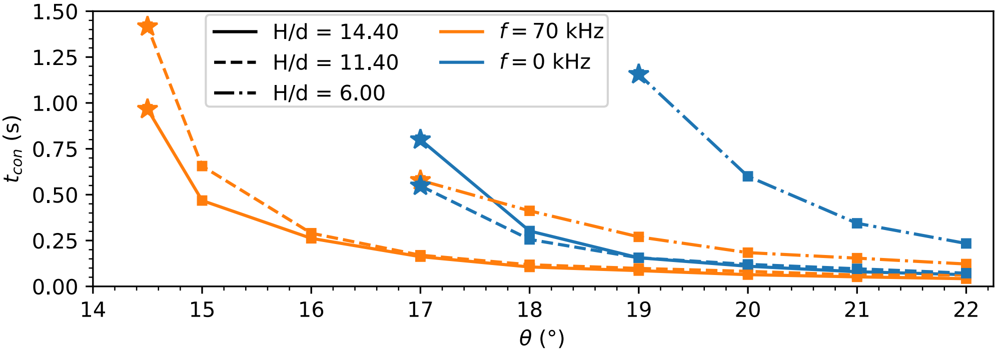

Figure 8: Delay time of avalanche triggering by gravity or (and) ultrasound vibration as a function of the slope angle for different thickness ratios H/d = 6, 11.4, and 14.4. The blue curves correspond to the measured times for flows without vibrations (f = 0 kHz), in contrast to the orange curves (f = 70 kHz). The stars indicate the maximum angles of stability corresponding to the avalanche angles measured for different thicknesses in Fig. 7 whereas the filled squares point to the inclined angles for which the flow has been initiated.

(or percolated; see Section 4.2), finally forming a *uniform* flowing mass. The normalized standard deviations σ_l of the grain velocity at the top (blue) and the bottom (red) layers, respectively, are shown in Figs. 6(b, d). These simulations illustrate that the avalanche angle is well around $\theta_m = 17°$. Indeed, at 0.8 s, the σ_l drop below the two criteria (Fig. 6(d)). Conversely, it is clear that at 16° the normalized standard deviations σ_l are far above the criteria for uniform flows (Fig. 6(b)).

Even when the whole flow reaches a high level of uniformity (both curves representing σ_l drop below the criteria), the flow uniformity in the top layer is larger than in the bottom layer, as the blue curve consistently remains below the red curve in Fig. 6(d). This behavior is consistently observed in all our simulations whatever the layer thickness and is consistent with the laboratory experiments of Bachelet *et al.* (2023) showing larger velocity fluctuations at the base of the flow.

Figure 7 highlights the avalanche angles for different thicknesses in the configuration where motion is solely generated by the inclination of the plane, i.e., without any basal vibrations. These angles represent the transition from a state where the granular mass is at rest (*jammed solid* state) to a *continuous flow* (for inclinations greater than the avalanche angle), sometimes passing from a metastable state that is not represented here. This boundary between the two limit states is depicted by the blue curve in a phase space composed, on the x-axis, of the inclination of the basal plane and, on the y-axis, of the average thickness of the granular mass in the initial state.

The shape of this blue curve (monotonic and decreasing) is similar to those reported in the literature (Daerr & Douady 1999; Forterre & Pouliquen 2002; Mangeney *et al.* 2010) showing that as the initial thickness increases, the avalanche angle decreases. The gray area represents the graph zone where the results strongly depend on the boundary conditions because the thickness of the granular layer is very thin (like $H = 3d$).

From angles greater than the avalanche angle θ_m, we measure the time t_{con} it takes for σ_l in the top and bottom layers to satisfy the criteria characterizing *uniform* flow. These times are represented in Fig. 8 for the three heights $H = 6d$, $11.4d$, and $14.4d$. The times t_{con} (without basal vibrations) represented by the blue curves are all decreasing. As expected, the larger the slope angle is, the shorter is the time required for the grains reach a *uniform* flow.

It is worth noting that the triggering duration decreases with the slope angle, but it seems

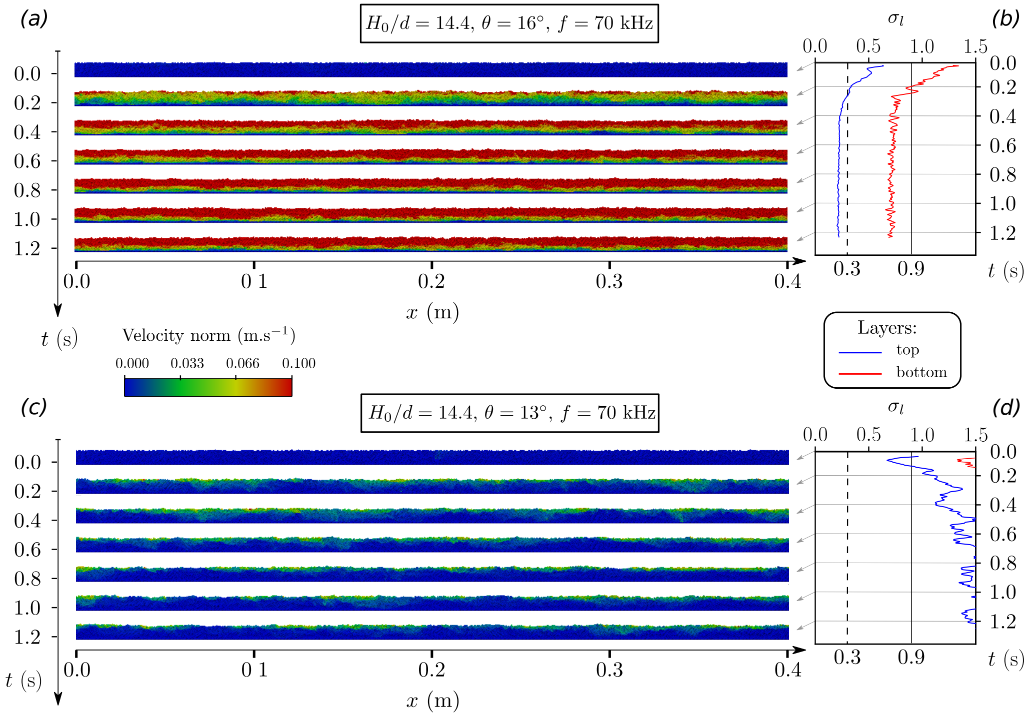

Figure 9: Granular assembly with basal vibrations ($f = 70$ kHz) at $\theta = 16°$ *(a, b)* and 13° *(c, d)* for $H = 14.4d$. *(a, c)* A sequence of 7 snapshots showing the evolution of a granular flow over time, ranging from $t = 0$ to 1.2 s. The color scale represents the magnitude of grain velocity. The observation domain covers a distance of 0.4 m and corresponds to the dashed rectangle in Fig. 5. *(b, d)* Variation, over the same time period, of the normalized standard deviation σ of grains' downslope velocity with respect to the average downslope velocity of the flow within two different layers decomposing the flow depth.

to converge to a limit beyond a certain slope angle, possibly due to the choice of the imposed criteria. This is reflected in Fig. 8 where the curves become almost horizontal for large angles. For example, for $H = 14.4d$, if the flow becomes *uniform* 0.5 s earlier by increasing the slope angle from 17° to 18°, it only becomes *uniform* 0.02 s earlier by increasing the slope angle from 21° to 22°. Finally, one might have expected a clear relationship between the inclination angle θ and the time t_{con} with the thickness of the granular layer H, but this is not what we observe here. In fact, while the thickness $H = 6d$ has a slower triggering time than the other two at 20°, indicating that the thinner thickness is slower, this is not the case at 17°, where the triggering for the largest thickness $H = 14.4d$ is faster than that for $11.4d$.

3.2. *Flow onset induced by vibration: transition to uniform flows via percolation*

In this section, we investigate the triggering of granular flows in the presence of basal vibrations at a frequency of 70 kHz. As described before, this triggering is modeled by coupling the COCD model (Section 2.1) with the steady *vibration model* (Section 2.2.2), through the modification of interparticle friction coefficients μ_p, which are altered by the vibrations using the *Mindlin model* (Section 2.3). More specifically, we observe how this basal vibration affects the results obtained without basal vibrations. Note that the basal vibration frequency $f = 70$ kHz is relatively high for a system with normal modes ranging from 1 kHz to 75 kHz, as shown in Fig. 3. We discuss this choice in Section 4.3.

Figures 9(a, b) present the same types of results as Figs. 6(a, b), decomposed into simulation snapshots and curves representing the temporal evolution of the σ_l in the top and bottom layers, still for a thickness of $H = 14.4d$. The difference here is that the basal vibration is on. Thus, at $\theta = 16°$, and contrary to the case without vibrations presented in Figs. 6(a, b), it is observed that a flow of the granular layer is triggered and converges towards a *continuous flow* after approximately $t = 0.25$ s (Fig. 9(a)). There is therefore a notable difference since only a part of the layer was flowing after 1.2 s in the case without vibrations (Figs. 6(a, b)). As a result, the avalanche angle θ_m is clearly lower in the case of basal vibrations compared to the case without. Similarly to the 17° angle without vibrations (Figs. 6(c, d)), the "top" layer is more *uniform* than the "bottom" layer, as indicated by the blue curve being significantly below the red curve (Fig. 9(b)). Unlike in the case without basal vibrations, we do not observe the initiation of flow occurring primarily at the front of the layer (low edge on the right in Fig. 6(c)). The mobilization of the granular layer is observed to be more *uniform* in the presence of vibrations. Another way to understand this is that the distinct triggering zones, which remain isolated for a considerable duration vibrations off, *percolate* much faster with vibrations on (see Section 4).

The decrease of avalanche angles due to vibration is observed in all simulations whatever the thickness and slope inclination, as shown in Fig. 7. Indeed, the orange curve, like the blue curve, is decreasing, but the important result here is that each of the avalanche angles in the orange curve (with vibrations) is lower than those in the blue curve by approximately 2°. The only notable singularity is the avalanche angle for the thin thickness $H = 3d$, which is only 14.5°, which is 5.5° smaller than in the case without basal vibrations. Such a difference can be explained by the dominance of boundary conditions as discussed in Section 4.

Let us now investigate what happens at smaller angles, *e.g.* at 13° but still for the thickness $H = 14.4d$, (Fig. 9(c, d)). Particularly visible in the snapshots (Fig. 9(c)), we observe that rearrangements are active, even at $t = 1.2$ s (some areas are light blue on the surface after 1.2 s). However, these rearrangements remain local and are not sufficient to trigger a flow that would develop into a *continuous flow*. This is confirmed by the values of σ_l, which both remain well below the criteria characterizing a *uniform* flow (Fig. 9(d)).

When the avalanche angle is exceeded, the effect of basal vibrations is to decrease the triggering time, as shown in Fig. 8. Indeed, for the same layer thickness, the triggering times represented by the orange curves are consistently lower than the triggering times without vibrations, i.e., the blue curves in Fig. 8. For example, for a thickness of $H = 6d$ and an angle $\theta = 19°$, the triggering time decreases by approximately 74 % (from $t_{con} = 1.15$ s without vibrations to only 0.3 s with vibrations). Similarly to the case without vibrations, the triggering times appear to converge to a limit but for angles much smaller (for $H = 11.4d$ and $14.4d$, the triggering times with vibrations are roughly the same at 18° as those at 22° without vibrations). Note that, once again, there is no clear influence of thickness on the triggering time.

4. Discussion

4.1. *Force chains, ultrasound-induced deformation, and lubricated contacts*

In the previous Section 3.2, we quantified how much basal ultrasonic vibrations reduces the avalanche angle and triggering time. We focus here on the interparticle mechanisms responsible for these effects, namely, the vibration-induced lubrication which is accounted for in our simulation by weakening of interparticle friction coefficients, as described by the *Mindlin model*(Section 2.3).

Figure 10 shows the grain configuration, at two consecutive times in the simulation $t =$

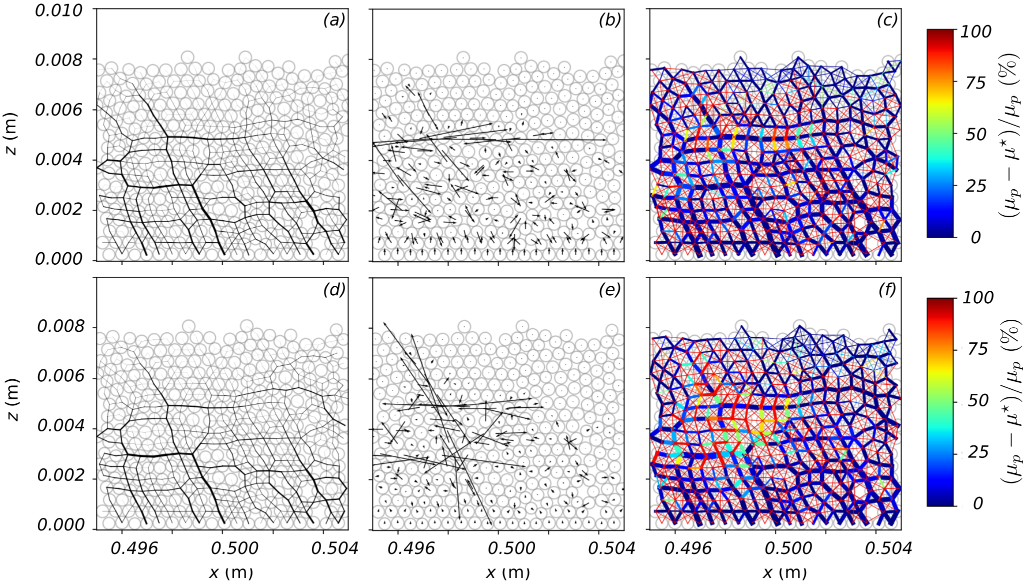

Figure 10: *(a, d)* Snapshots of the contact force chains, *(b, e)* vibration-induced displacements, and *(c, f)* rate of vibration-induced perturbation of the interparticle friction, for $\theta = 15°$, $H/d = 14.4$, $f = 70\,\mathrm{kHz}$. In *(a, d)*, the black lines represent the force chains formed between the grains on a linear scale (the coefficients f_n^{ij} in Section 2.2.2). In *(b, e)*, the black arrows represent the computed vibration-induced displacement $\boldsymbol{q}$ in Eqs. (2.10)-(2.11) (but not at the same scale). In *(c, f)*, the lines between grains represent the force chains on a logarithmic scale, and the color map represent the rate of decrease in interparticle friction coefficients, i.e., the quantity $(\mu_p - \mu_{ij}^\star)/\mu_p$ (see Eq. (2.12)). Snapshot times are $t = 0.051$ s *(a)-(c)* and $t = 0.052$ s *(d)-(f)*.

0.051 s and 0.052 s (the numerical time step is $\Delta t_g = 1$ ms) for a slope angle $\theta = 15°$, a layer thickness $H = 14.4d$ and in a region between $x = 0.497$ and 0.505 m. The black lines in Figs. 10(a, d) represent the force chains formed between the grains (their width correspond to normal force intensities f_n^{ij} (see Section 2.1)). The arrows shown in Figs. 10(b, e) represent the deformation fields computed with the steady *vibration model* (the vector $\boldsymbol{q} \in \mathbb{R}^{3N}$ solution to Eqs. (2.10)-(2.11)). Note that the layer of grains in contact with the bottom has a unit displacement of 1, but for the sake of visibility of the deformation field, we did not use the same scale in Figs 10(b, e), 12(b), and 13(b, e, h, k). The force chains are again depicted in Figs. 10(c, f), but on a logarithmic scale (which explains the different thicknesses compared to the linear scale in Figs. 10(a, d). The colors represent the rate of change of interparticle friction coefficients, i.e., the quantity $(\mu_p - \mu_{ij}^\star)/\mu_p$ (see Eq. (2.12)). Where the force chains are blue, the coefficients are slightly modified, while where they are red, the coefficients are reduced to zero (thus decreased by 100 %). Figure 10 illustrates two destabilization mechanisms of the granular layer revealed by our simulations.

The first mechanism, presented in Figs. 10(a)-(c), involves the transmission of deformation induced by basal vibrations in a preferential direction (in this case, horizontal around $z = 0.005$ m and between $x = 0.496$ and 0.501 m) through a relatively dominant (strong) force chain in the corresponding region (thicker force chain in this particular region (Fig. 10(a))). This transmission only slightly affects the interparticle friction coefficients along this force chain (the horizontal force chain appears as dark blue in Fig. 10(c)). On the contrary, the

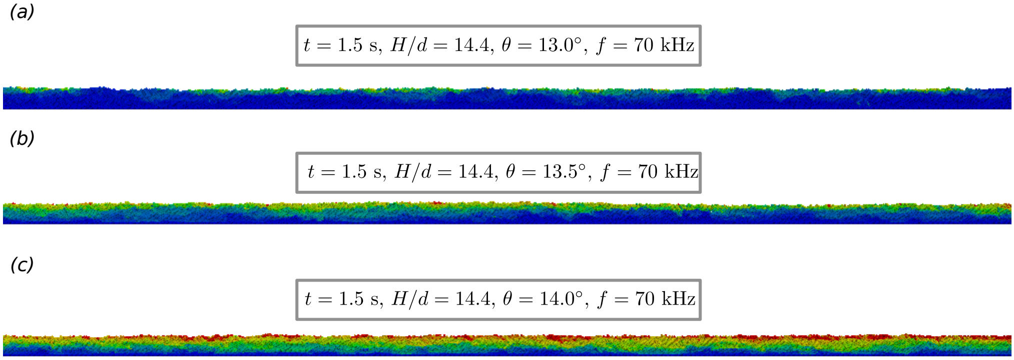

Figure 11: The percolation transition is accelerated with the presence of basal ultrasound vibrations when increasing the slope angle.

friction coefficients on contacts relatively perpendicular to this main force chain significantly changed (bright colors for vertical force chains surrounding the main force chain in Fig. 10(c)).

A second mechanism revealed by our simulations involves a kind of block destabilization. This mechanism is presented in Figs. 10(d)-(f). In this case, the destabilization does not follow a preferred direction but occurs in multiple directions (Fig. 10(e)), while remaining localized in a specific area of the granular layer (between $z = 0.002$ and 0.006 m and $x = 0.496$ and 0.501 m in Fig. 10(d)). A few strong force chains are present in this area (Fig. 10(d)), but the friction coefficients are primarily modified on the less dominant (weak) force chains within the disturbed zone (Fig. 10(f)). Note that the different response of weak and strong force chains when getting close to instability was also observed in Deboeuf *et al.* (2005).

In our simulations, we have noticed that the first mechanism (destabilization along a preferred direction) can trigger the second mechanism, as seen here since the figures are taken at consecutive times. However, this is not always the case. Sometimes, only the first or the second mechanism occurs. We have not observed that the second mechanism can trigger the first mechanism.

4.2. *Nucleation time (delay) to reach uniform flows*

When the basal plane is inclined, localized rearrangement zones appear both with and without vibrations (Figs. 6(a, c), and 9(a, c)). Without vibrations, these zones can remain isolated for a significant period if the slope is not too steep (Fig. 6(a)). However, beyond the avalanche angle, they can eventually merge (or "percolate") and result in a relatively *uniform* flow (Fig. 6(c)). In simulations with vibrations, in addition to this triggering mechanism through inclination, there are also interparticle vibratory mechanisms that trigger specific zones within the granular layer (Fig. 10). The difference with vibrations is that the triggering zones are much more numerous and percolate much faster (Figs. 9(a) and 8), leading to a quick homogenization of the flow (Fig. 9(b)) and resulting in lower avalanche angles compared to cases without vibrations (Fig. 7). In our simulations, this phenomenon of *percolation transition* is faster and more *uniform* with vibrations on, and it increases with the slope, as shown in Fig 11.

4.3. *Basal vibration frequency and amplitude*

The ultrasound basal vibration has a quite high frequency ($f = 70$ kHz) when compared to the system normal modes, which are mostly comprised between 5 kHz to 45 kHz (Fig. 3). In our simulations, the disturbance is more effective when the frequency is well-centered within the

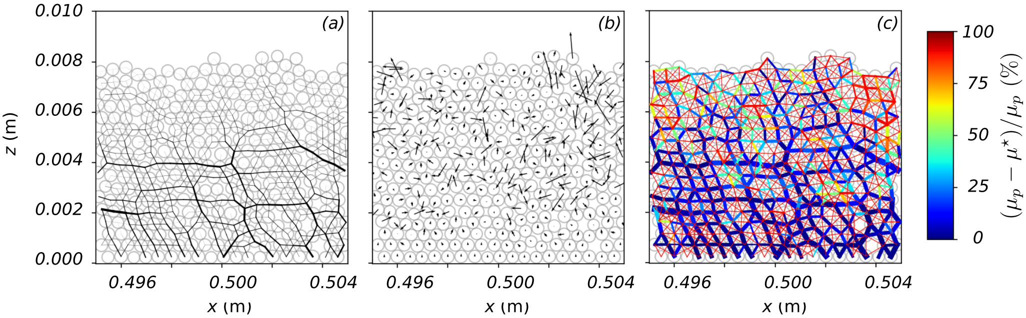

Figure 12: *(a)* Snapshots of the contact force chains, *(b)* vibration-induced displacements, and *(c)* rate of vibration-induced perturbation of the interparticle friction, for $\theta = 15°,\ H/d = 14.4,\ f = 30\,\mathrm{kHz}$, at $t = 0.072\,\mathrm{s}$. *(a)* The black lines represent the force chains formed between the grains on a linear scale (the coefficients f_n^{ij} in Section 2.2.2). *(b)* The black arrows represent the computed vibrational displacement $\boldsymbol{q}$ in Eqs. (2.10)-(2.11). *(c)* The lines between grains represent the force chains on a logarithmic scale, and the color map represent the rate of decrease in interparticle friction coefficients, i.e., the quantity $(\mu_p - \mu_p^\star)/\mu_p$ (see Eq. (2.12)). The basal vibration amplitude is the same as in Fig. 10, about $U_0/d = 10^{-5}$.

medium's spectrum and the results presented are qualitatively similar at a lower frequency. For example, the simulation we conducted with $f = 30\,\mathrm{kHz}$ shows a more significant and less localized disturbance of friction coefficients (Fig.12). Figure 12 highlights that the fundamental disturbance was transmitted more effectively from the bottom of the medium to the grains in the upper layers, and this was achieved more efficiently than at the higher frequency of 70 kHz (Fig. 10).

Regarding the choice of the amplitude of the basal vibration U_0, we used the same amplitude for all simulations, $U_0/d = 10^{-5}$, which is equivalent to a few tens of nanometers. Figure 13 illustrates the effects of the ultrasonic vibrations on the coefficients of friction for the same frequency, $f = 70\,\mathrm{kHz}$, but with amplitude U_0 ranging from $U_0/d = 10^{-3}$ to $U_0/d = 10^{-6}$. It can be observed that, even though the solution of the steady problem remains similar in terms of the distribution of perturbations (Figs. 13(b, e, h, k)), simulations conducted with larger amplitudes significantly alter the friction coefficients, obviously more than those with smaller amplitudes (Figs.13(c, f, i, l)). Furthermore, the choice of amplitude made in this article corresponds to an amplitude so small that the perturbations, although non-zero, remain small and generally localized (Fig.13(i)).

By making these choices of frequency and amplitude of the ultrasound, we deliberately positioned the numerical simulations in an amplitude-frequency regime that makes disturbing the medium the most challenging, without inducing significant rearrangement of grain positions. The high-frequency domain is less explored than that of low-frequency vibrations, which are already well-known for their significant triggering effects, e.g., see (Hanotin *et al.* 2012; Lastakowski *et al.* 2015). Decreasing (respectively increasing) the value of the basal vibration frequency (respectively amplitude) does not qualitatively alter the results presented in this article. The coupling of numerical models we present in this article is relevant in a frequency range from 5 kHz to 80 kHz (Fig. 3) and with amplitudes ranging from $10^{-6}d$ to $10^{-2}d$. We have not conducted studies beyond this range of parameters, but our model is likely to be less relevant in those cases since consideration of grain displacement at very low frequencies and/or large amplitudes may be necessary; see, e.g., (Baumberger & Caroli 2006; Bureau *et al.* 2001; Hanotin *et al.* 2012).

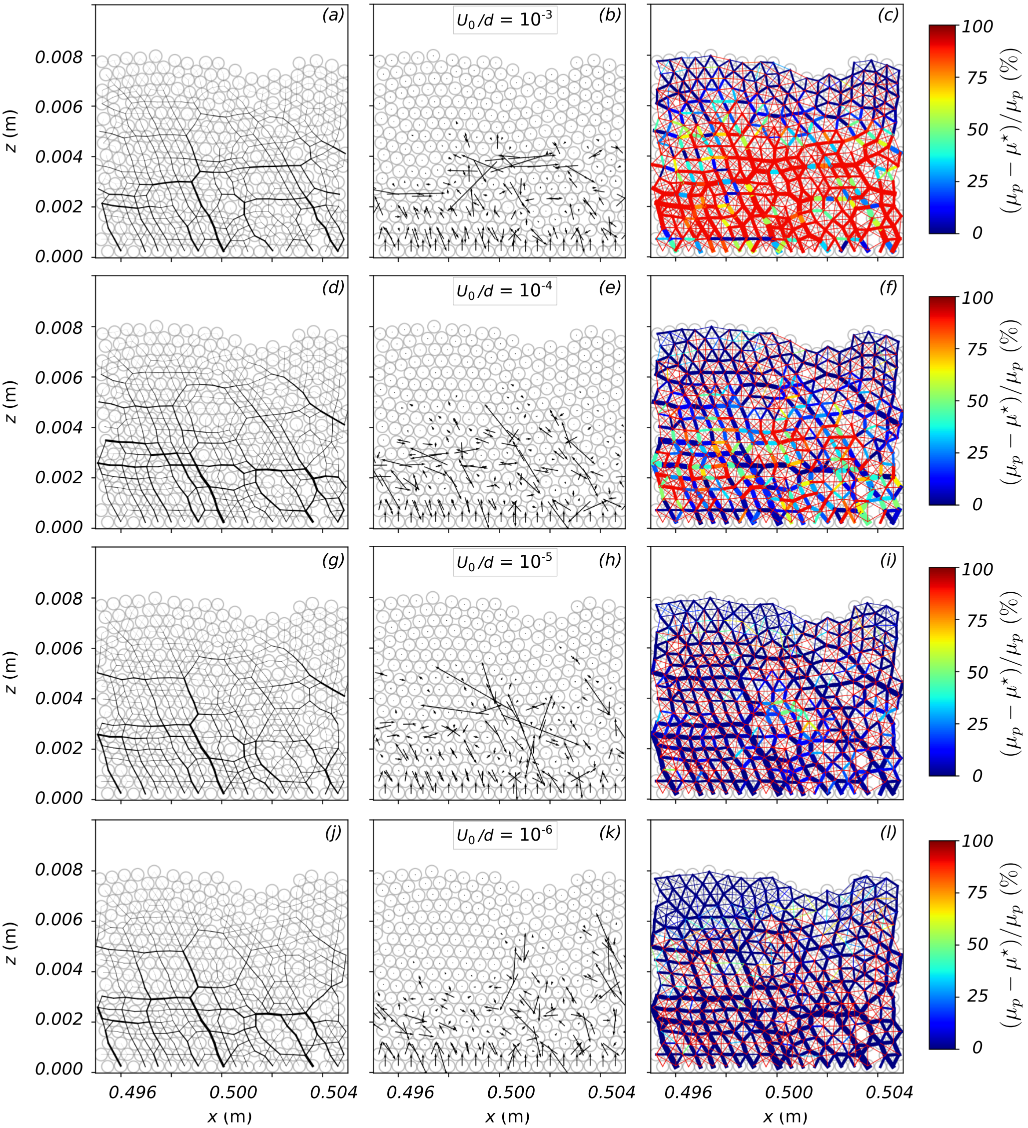

Figure 13: *(a, d, g, j)* Snapshots of the contact force chains, *(b, e, h, k)* vibration-induced displacements (normalized by the basal amplitude), and *(c, f, i, l)* rate of vibration-induced perturbation of the interparticle friction, for $\theta = 15^\circ$, $H/d = 14.4$, $f = 70\,\text{kHz}$, and amplitudes $U_0/d = 10^{-n}$, for $n = 3\ldots6$, at $t = 0.018\,\text{s}$.

4.4. *Comparison with laboratory experiments: boundary effects*

Finally, we investigate the boundary effect on the granular flows, driven by gravity or triggered by ultrasound, and compare the simulations with the experiments realized under similar conditions. Figure 14(a) demonstrates how basal vibrations transition the triggering mechanism from being predominantly at the front of the granular layer to being uniformly distributed throughout the entire domain (Fig. 14(b)). Without vibrations, the velocities of grains represented by the red arrows are mostly large towards the front and small towards the back (Fig. 14(a)). Conversely, with vibrations on, the velocities are roughly the same magnitude across the entire domain (Fig. 14(b)).

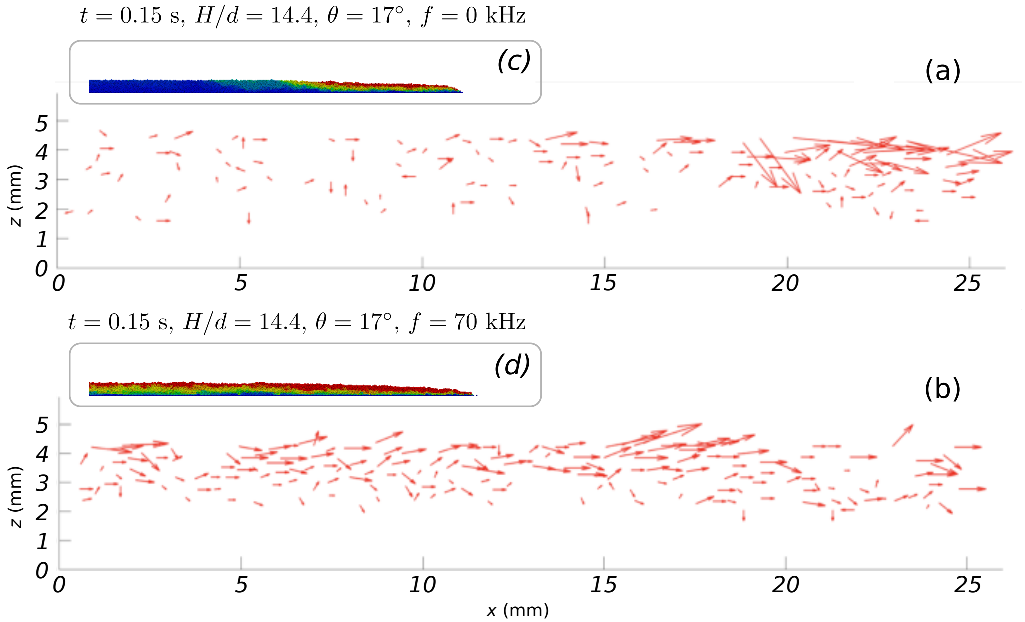

Figure 14: Experimental velocity fields of granular flows (side view) in a dry packing during the first 0.15 s interval: *(a)* driven by gravity at the avalanche angle $\theta_m = 24° \pm 1°$. *(b)* Triggered by ultrasounds at $\theta = 22°$. *(c)* Simulation snapshot at the front for $\theta_m = 17°,\ H/d = 14.4,\ f = 0\,\text{kHz}$, at $t = 0.15$ s. *(d)* Simulation triggered by ultrasounds ($f = 70\,\text{kHz}$).

In addition, in our simulations, the front systematically starts moving when the avalanche angle is exceeded (as illustrated in the inset Fig. 14(c), which shows the granular front, i.e., the right end of the mass in Fig. 5). Similarly, the experimental data also exhibit a configuration of a granular mass flowing near the front (Fig. 14(a)). In both experiments and simulations, we observe that vibration-triggered flows are more *uniform* (Figs. 14(b, d)) than the ones induced by gravity only (Figs. 14(a, c)).

Thus, we believe that the additional triggering mechanisms associated with basal vibrations, even if they are infinitesimal (ultrasounds in this article and in the experiments), are sufficient to uniformly destabilize the granular layer and consequently lead to a more *uniform* destabilization, resulting in a reduction of the avalanche angle of the mass.

5. Conclusion

In summary, we have developed a two-time scale numerical simulation of wave-induced friction weakening in 2D granular layers. Indeed ultrasound vibrations propagate with a time-scale of the order of 10 microseconds while grain motion occur at a time-scale of milliseconds. The triggering of granular flows is modeled by coupling the COCD model (Section 2.1) with the steady *vibration model* (Section 2.2.2), through the modification of interparticle friction coefficients μ_p, which are altered by the vibrations using the *Mindlin model* (Section 2.3). This new two-time scale model has allowed us to investigate the nonlinear interaction between ultrasound and granular flows, in particular the vibration-induced reduction of the interparticle friction coefficient through the acoustic lubrication, without the contact opening and rearrangements of grain positions.

As expected, we find that ultrasound vibration is predominantly supported by the strong-force chains, but the vibration-induced decrease of friction occurs mainly in the weak-force chains perpendicular to the strong contact forces, causing eventually STZ-like zones (shear transformation zones) on the mescoscopic scale. These local rearrangements nucleate to create a continuous flow through a percolation process with certain delay depending on the proximity to the failure, i.e. avalanche angles. The larger the vibration amplitude (or lower excitation frequency) is, the stronger the ultrasound induced destabilization is. The different in the behaviour of weak and strong force chains was also observed in the response of a granular packing (without vibration) during successive loading-unloading cycles close to the avalanche angle (Deboeuf *et al.* 2005).

Compared to gravity-driven flow, ultrasound-induced flow appears more spatially homogeneous. This is consistent with the effective temperature role played by sound vibration. The qualitative agreement between these simulations and experimental observations of granular flows triggered by ultrasound supports our numerical modeling. Although further improvement on the vibration model is still needed, this work helps to highlight underlying mechanisms of landslide and earthquake triggering by seismicity; see, *e.g.,* Durand *et al.* (2023).

Acknowledgements. We thank MOSEK APS (2010) for the free academic license that made this article possible.

Funding. This article has been funded by the ERC Contract No. ERC-CG-2013-PE10-617472 SLIDE-QUAKES.

Declaration of interests. The authors report no conflict of interest.

Author ORCIDs. H. A. Martin, https://orcid.org/0000-0002-7089-8958; A. Mangeney, https://orcid.org/0000-0002-3197-6087; X. Jia, https://orcid.org/0000-0003-0874-8235; B. Maury, https://orcid.org/0000-0001-5474-4134; A. Lefebvre-Lepot, https://orcid.org/0000-0002-9521-126X; Y. Maday, https://orcid.org/0000-0002-0443-6544; P. Dérand, https://orcid.org/0009-0003-0166-006X

Author contributions. H. A. Martin: Conceptualization, Methodology, Software, Writing – original draft. A. Mangeney: Conceptualization, Funding acquisition, Methodology, Project administration, Supervision, Writing – original draft. X Jia: Conceptualization, Methodology, Experiment, Supervision, Writing – original draft. B. Maury: Conceptualization, Methodology, Supervision, Writing – original draft. A. Lefebvre-Lepot: Conceptualization, Methodology, Supervision, Writing – original draft. Y. Maday: Conceptualization, Funding acquisition, Methodology, Project administration, Supervision, Writing – original draft. P. Dérand: Conceptualization, Methodology, Experiment.

Appendix A. Wave equation

The purpose of this section is to present the derivation of the *wave equation* introduced by Eq. (2.9). We model the time-evolution of an infinitesimal perturbation of a given configuration $\boldsymbol{c}^0 \in \mathbb{R}^{3N}$ (the generalized position vector), supposed to be at rest. We first introduce a few elements of the Hertz theory in Section A.1. In Section A.2, we describe the way the resulting perturbation of the overlaps δ_{ij} is handled and its implication on the set of contact forces. Then, we show how this perturbation is related to the configuration itself in Section A.3 and derive the *wave equation* in Section A.4.

A.1. *Embedding Hertz theory*

In Section 2.2.2, the normal force between two grains i and j is characterized, at the local scale, by a positive scalar $f_n^{ij} > 0$. The Hertz theory of contact provides a useful framework to model an elastic force at a contact between two particles. The general expression of the Hertz normal force between two grains is

$$F_n = \kappa_{ij}\delta_{ij}^{3/2}, \tag{A 1}$$

where κ_{ij} is a constant depending on grains' properties and δ_{ij} is the overlap between the particles i and j, characterizing grains deformation.

Note the difference between the distances D_{ij}, defined in Eq. (2.1) and δ_{ij}: on the one hand, the distance D_{ij} measures how far the grains are from each other, on the other hand, the overlap δ_{ij} models an overlap between the grains i and j, which should be seen as quantifying a deformation of the bodies now considered as elastic. The two terms D_{ij} and δ_{ij} evolve in opposite way. When the distance D_{ij} between i and j increases their overlap δ_{ij} decreases. The scalars f_n^{ij} can be provided by any model like COCD, as being the normal intensity of the contact force, while F_n is the normal force intensity in the Hertz theory framework.

The prefactor can be found from the Hertz theory of elastic contact (see the book of Andreotti, Forterre, and Pouliquen Andreotti *et al.* (2013) and the book of Johnson Johnson (2014)). In the case of a contact between two spheres i and j of radii r_i, r_j, Young's moduli E_i, E_j, and Poisson's ratios ν_i, ν_j, we have $\kappa_{ij} = (4/3)E_{ij}\sqrt{r_{ij}}$, where E_{ij} and r_{ij} are defined by $1/E_{ij} = (1-\nu_i^2)/E_i + (1-\nu_j^2)/E_j$ and $1/r_{ij} = 1/r_i + 1/r_j$. However, to compare qualitatively the sound speed or elastic modulus of granular layers measured in laboratory experiments (see discussions in Section 2) with the present simplified Hertz (normal) contact model, we would need to upscale uniformly the coefficients κ_{ij} by a factor of 100. This scaling does not qualitatively affect the results presented in this article since the basal vibration frequency is chosen with respect to the system normal modes; see Section 2.

A.2. *First order Taylor expansion of Hertz contact force*

Let J_c be the set of contacts defined by $J_c = \{(i,j) \mid 1 \leqslant i < j \leqslant N \quad \text{and} \quad \exists f_n^{0\,ij} > 0\}$. We denote by N_c the cardinal of set J_c. Let us assume to be given a generalized normal force intensity vector $\boldsymbol{f}^0 \in \mathbb{R}^{N_c}$, where $f_n^{0\,ij} > 0$, for any $(i,j) \in J_c$. We can define the overlap δ_{ij}^0 by

$$\delta_{ij}^0 = \left(\frac{f_n^{0\,ij}}{\kappa_{ij}}\right)^{2/3}. \tag{A 2}$$

We assume that the quantities $f_n^{0\,ij}$ and δ_{ij}^0 remain constant at the *vibration time scale* and we study the effects of small perturbations around this equilibrium. We denote by $\varepsilon_{ij} \in \mathbb{R}$, the *infinitesimal perturbation* of δ_{ij}^0 and the *perturbation-induced* overlap by $\delta_{ij} \in \mathbb{R}$, such that we have by definition

$$\delta_{ij} = \delta_{ij}^0 + \varepsilon_{ij}. \tag{A 3}$$

Only δ_{ij} and ε_{ij} depend on time while δ_{ij}^0 remains constant. Consequently, when considering the *perturbation-induced* overlap δ_{ij}, a Taylor expansion at the first order of Eq. (A 2) provides the value of a *perturbation-induced* normal force intensity, denoted by $f_n^{ij} \in \mathbb{R}$. This can be formalized by

$$\begin{aligned} f_n^{ij} &= \kappa_{ij}\left(\delta_{ij}\right)^{3/2} \\ &= \kappa_{ij}\left(\delta_{ij}^0 + \varepsilon_{ij}\right)^{3/2} \\ &= \kappa_{ij}(\delta_{ij}^0)^{3/2} + \frac{3}{2}\kappa_{ij}(\delta_{ij}^0)^{1/2}\varepsilon_{ij} + o\left(\frac{\varepsilon_{ij}}{\delta_{ij}^0}\right), \\ &\simeq f_n^{0\,ij} + \underbrace{\frac{3}{2}\kappa_{ij}(\delta_{ij}^0)^{1/2}\varepsilon_{ij}}_{=f_n^{\varepsilon\,ij}} \end{aligned} \tag{A 4}$$

and where the term $f_n^{\varepsilon\,ij}$ is the *infinitesimal perturbation* of $f_n^{0\,ij}$ and plays for the *perturbation-induced* force f_n^{ij} the role played by the term ε_{ij} for δ_{ij} in Eq. (A 3).

A.3. *Perturbation-induced position vector*

We now consider given a generalized position vector of the mechanical system at the equilibrium that we denote $\boldsymbol{c}^0 \in \mathbb{R}^{3N}$; see Section 2.1. In the previous section, the *perturbation-induced* force f_n^{ij} can be expressed as a linear function of the *infinitesimal perturbation* ε_{ij} of the overlap δ_{ij}^0 (see Eq. A 3). Similarly, we define the *perturbation-induced* position vector $\boldsymbol{c}$ and $\boldsymbol{e}$, the *infinitesimal perturbation* of the constant position vector $\boldsymbol{c}^0$, all belonging to $\mathbb{R}^{3N}$, i.e.,

$$\boldsymbol{c} = \boldsymbol{c}^0 + \boldsymbol{e},$$

where, at the *vibration time scale*, $\boldsymbol{c}$ and $\boldsymbol{e}$ depend on time while $\boldsymbol{c}^0$ remains constant. We can write ε_{ij}, the *infinitesimal perturbation* of the overlap δ_{ij}^0 as the image of $\boldsymbol{e}$ by the map $\boldsymbol{N}_{ij}$, indeed, we have

$$\varepsilon_{ij} = (\delta_{ij} - \delta_{ij}^0) = -((\boldsymbol{c}_i - \boldsymbol{c}_j) - (\boldsymbol{c}_i^0 - \boldsymbol{c}_j^0)) \cdot \boldsymbol{n}_{ij} = -\left(\boldsymbol{e}_i - \boldsymbol{e}_j\right) \cdot \boldsymbol{n}_{ij} = -\boldsymbol{N}_{ij}\boldsymbol{e}. \tag{A 5}$$

We define also the *perturbation-induced* generalized force intensity vector $\boldsymbol{f} \in \mathbb{R}^{N_c}$, resulting from the perturbation of the constant vector $\boldsymbol{f}^0 \in \mathbb{R}^{N_c}$ by the *infinitesimal perturbation* vector $\boldsymbol{f}^\varepsilon \in \mathbb{R}^{N_c}$, i.e.,

$$\boldsymbol{f} = \boldsymbol{f}^0 + \boldsymbol{f}^\varepsilon.$$

Equations (A 2), (A 4), and (A 5) give $f_n^{\varepsilon\,ij} = -3/2(\kappa_{ij})^{2/3}\left(f_n^{0\,ij}\right)^{1/3}\boldsymbol{N}_{ij}\boldsymbol{e}$, which can be written under its vector form as

$$\boldsymbol{f}^\varepsilon = -\boldsymbol{K}\boldsymbol{N}\boldsymbol{e} \in \mathbb{R}^{N_c},$$

where the diagonal square matrix $\boldsymbol{K}$ contains the elastic properties of the system:

$$\begin{aligned} \boldsymbol{K} = \frac{3}{2}\mathrm{diag}\Bigg((\kappa_{1,2})^{2/3}\left(f_n^{0\,1,2}\right)^{1/3}, \dots \\ \dots, (\kappa_{ij})^{2/3}\left(f_n^{0\,ij}\right)^{1/3}, \dots \\ \dots, (\kappa_{N-1,N})^{2/3}\left(f_n^{0\,N-1,N}\right)^{1/3}\Bigg) \in \mathbb{R}^{N_c \times N_c}, \end{aligned}$$

A.4. *Wave equation*

The assumption is made on the system described in Section 2.1 to be at rest, maintained by the gravity field. In this configuration, Newton's second law imposes that there exists a generalized reaction force vector that is necessary opposed to the global force vector $\boldsymbol{w}^0 = (\boldsymbol{w}_1^0, \ldots, \boldsymbol{w}_N^0) \in \mathbb{R}^{3N}$, applied on the system. Coupled with the non-overlapping condition $\mathrm{D}_{ij} \geqslant 0$, it is equivalent to say that the inverse image of the vector $-\boldsymbol{w}^0$ by the map $\boldsymbol{N}^T$ (see Section 2.2.1), intersected with $\mathbb{R}_+^{N_c}$ (to have repulsive force only) is not empty, i.e., ${\boldsymbol{N}^T}^{-1}(-\boldsymbol{w}^0) \cap \mathbb{R}_+^{N_c} \neq \varnothing$. Let the generalized normal force intensity vector $\boldsymbol{f}^0 \in \mathbb{R}_+^{N_c}$, belonging to the inverse image of the vector $-\boldsymbol{w}^0$ by the map $\boldsymbol{N}^T$, we have

$$\boldsymbol{N}^T \boldsymbol{f}^0 = -\boldsymbol{w}^0 \in \mathbb{R}^{2N},$$

whose local expression is exactly given by Eq. (2.7). The generalized force vector $\boldsymbol{N}^T \boldsymbol{f}^0$ generates local normal repulsive forces between the spheres at the contact points. Furthermore, the generated pressures create deformation zones and the Hertz theory enables us to characterize these deformations by a set of scalars $\delta_{ij}^0 \in \mathbb{R}$ (see Eq.(A 1)). Consequently, the δ_{ij}^0 can be given by an equation of type Eq. (A 2). As a result, we have shown how the forces computed at the *grain-motion time scale* by the *grain-motion model* COCD, which does not involve the Hertz theory can be linked to the latest at the *vibration time scale*, through the introduction of the overlaps δ_{ij}^0.

With the generalized mass matrix (masses only) defined by Eq. (2.8), and by considering the *perturbation-induced* generalized force vector $\boldsymbol{N}^T \boldsymbol{f} \in \mathbb{R}^{3N}$, and applying Newton's second law, we finally obtain the unsteady wave equation resulting from the perturbation of $\boldsymbol{c}^0$ by $\boldsymbol{e}$. Indeed, we have

$$\begin{aligned} \bar{\boldsymbol{M}} \frac{\mathrm{d}^2 \boldsymbol{c}}{\mathrm{d}t^2} = \boldsymbol{N}^T \boldsymbol{f} + \boldsymbol{w}^0 \iff \bar{\boldsymbol{M}} \frac{\mathrm{d}^2 \boldsymbol{e}}{\mathrm{d}t^2} &= \boldsymbol{N}^T (\boldsymbol{f}^0 + \boldsymbol{f}^\varepsilon) + \boldsymbol{w}^0 \\ \bar{\boldsymbol{M}} \frac{\mathrm{d}^2 \boldsymbol{e}}{\mathrm{d}t^2} &= -\boldsymbol{N}^T \boldsymbol{K} \boldsymbol{N} \boldsymbol{e}. \end{aligned}$$

At the end, a *wave equation* is defined for any $\boldsymbol{e} \in \mathbb{R}^{3N}$

$$\bar{\boldsymbol{M}} \frac{\mathrm{d}^2 \boldsymbol{e}}{\mathrm{d}t^2} + \boldsymbol{\Lambda} \boldsymbol{e} = 0,$$

where the linear map defined by the matrix

$$\boldsymbol{\Lambda} = \boldsymbol{N}^T \boldsymbol{K} \boldsymbol{N} \in \mathbb{R}^{3N \times 3N},$$

can be seen as a kind of discrete Laplace operator.

REFERENCES

Acary, V., Cadoux, F., Lemaréchal, C. & Malick, J. 2011 A formulation of the linear discrete Coulomb friction problem via convex optimization. *ZAMM Zeitschrift fur Angewandte Mathematik und Mechanik* **91** (2), 155–175.

Andreotti, B., Forterre, Y. & Pouliquen, O. 2013 *Granular Media: Between Fluid and Solid*. Cambridge, UK: Cambridge University Press.

Anitescu, Mihai 2006 Optimization-based simulation of nonsmooth rigid multibody dynamics. *Mathematical Programming* **105** (1), 113–143.

Bachelet, V., Mangeney, A., Toussaint, R., de Rosny, J., Arran, M. I., Farin, M. & Hibert, C. 2023 Acoustic emissions of nearly steady and uniform granular flows: A proxy for flow dynamics and velocity fluctuations. *Journal of Geophysical Research: Earth Surface* **128** (4), e2022JF006990.

BALDASSARRI, A., DALTON, F., PETRI, A., ZAPPERI, S., PONTUALE, G. & PIETRONERO, L. 2006 Brownian Forces in Sheared Granular Matter. *Physical Review Letters* **96** (11), 118002.

BAUMBERGER, T. & CAROLI, C. 2006 Solid friction from stick–slip down to pinning and aging. *Advances in Physics* **55** (3-4), 279–348.

BLOCH, HELENE & LEFEBVRE-LEPOT, ALINE 2023 On convex numerical schemes for inelastic contacts with friction. In *ESAIM: Proceedings and Surveys* (ed. Marie Doumic, Sébastien Gadat & Quentin Mérigot), , vol. 75, pp. 24–59.

BONNEAU, L., ANDREOTTI, B. & CLÉMENT, E. 2008 Evidence of rayleigh-hertz surface waves and shear stiffness anomaly in granular media. *Phys. Rev. Lett.* **101**, 118001.

BOUCHON, M., DURAND, V., MARSAN, D., KARABULUT, H. & SCHMITTBUHL, J. 2013 The long precursory phase of most large interplate earthquakes. *Nature geoscience* **6** (4), 299–302.

BRUM, J., GENNISSON, J., FINK, M., TOURIN, A. & JIA, X. 2019 Drastic slowdown of the rayleigh-like wave in unjammed granular suspensions. *Phys. Rev. E* **99**, 042902.

BUREAU, L., BAUMBERGER, T. & CAROLI, C. 2001 Jamming creep of a frictional interface. *Physical Review E* **64** (3), 031502.

CLEMENT, E. & RAJCHENBACH, J. 1991 Fluidization of a Bidimensional Powder. *Europhysics Letters (EPL)* **16** (2), 133–138.

COCHARD, A., BUREAU, L. & BAUMBERGER, T. 2003 Stabilization of Frictional Sliding by Normal Load Modulation. *Journal of Applied Mechanics* **70** (2), 220–226.

COUSSOT, P., NGUYEN, Q. D., HUYNH, H. T. & BONN, D. 2002 Avalanche Behavior in Yield Stress Fluids. *Physical Review Letters* **88** (17), 175501.

COUTO, R. T. 2013 Green's functions for the wave, Helmholtz and Poisson equations in a two-dimensional boundless domain. *Revista Brasileira de Ensino de Física* **35** (1), 01–08.

CUNDALL, P. A. & STRACK, O. D. L. 1979 A discrete numerical model for granular assemblies. *Géotechnique* **29** (1), 47–65.

DAERR, A. & DOUADY, S. 1999 Two types of avalanche behaviour in granular media. *Nature* **399** (6733), 241–243.

D'ANNA, G., MAYOR, P., BARRAT, A., LORETO, V. & NORI, F. 2003 Observing brownian motion in vibration-fluidized granular matter. *Nature* **424** (6951), 909–912.

DEBOEUF, S., DAUCHOT, O., STARON, L., MANGENEY, A. & VILOTTE, J.-P. 2005 Memory of the unjamming transition during cyclic tiltings of a granular pile. *Phys. Rev. E* **72**, 051305.

DIJKSMAN, J. A., WORTEL, G. H., VAN DELLEN, L. T. H., DAUCHOT, O. & VAN HECKE, M. 2011 Jamming, Yielding, and Rheology of Weakly Vibrated Granular Media. *Physical Review Letters* **107** (10), 108303.

DURAND, V., MANGENEY, A., BERNARD, P., JIA, X., BONILLA, F., SATRIANO, C., SAUREL, J., AISSAOUI, E., PELTIER, A., FERRAZZINI, V., KOWALSKI, P., LAURET, F., BRUNET, C. & HIBERT, C. 2023 Repetitive small seismicity coupled with rainfall can trigger large slope instabilities on metastable volcanic edifices. *Communications Earth & Environment* **4** (1), 383.

DURAND, V., MANGENEY, A., HAAS, F., JIA, X., BONILLA, F., PELTIER, A., HIBERT, C., FERRAZZINI, V., KOWALSKI, P., LAURET, F., BRUNET, C., SATRIANO, C., WEGNER, K., DELORME, A. & VILLENEUVE, N. 2018 On the Link Between External Forcings and Slope Instabilities in the Piton de la Fournaise Summit Crater, Reunion Island. *Journal of Geophysical Research: Earth Surface* **123** (10), 2422–2442.

FORTERRE, YOËL & POULIQUEN, OLIVIER 2002 Stability analysis of rapid granular chute flows: formation of longitudinal vortices. *Journal of Fluid Mechanics* **467**, 361–387.

GOMBERG, J., REASENBERG, P. A., BODIN, P. & HARRIS, R. A. 2001 Earthquake triggering by seismic waves following the Landers and Hector Mine earthquakes. *Nature* **411** (6836), 462–466.

HANOTIN, C., KIESGEN DE RICHTER, S., MARCHAL, P., MICHOT, L. J. & BARAVIAN, C. 2012 Vibration-induced Liquefaction of Granular Suspensions. *Physical Review Letters* **108** (19), 198301.

HILL, D. P., REASENBERG, P. A., MICHAEL, A., ARABAZ, W. J., BEROZA, G., BRUMBAUGH, D., BRUNE, J. N., CASTRO, R., DAVIS, S., DEPOLO, D., ELLSWORTH, W. L., GOMBERG, J., HARMSEN, S., HOUSE, L., JACKSON, S. M., JOHNSTON, M. J. S., JONES, L., KELLER, R., MALONE, S., MUNGUIA, L., NAVA, S., PECHMANN, J. C., SANFORD, A., SIMPSON, R. W., SMITH, R. B., STARK, M., STICKNEY, M., VIDAL, A., WALTER, S., WONG, V. & ZOLLWEG, J. 1993 Seismicity Remotely Triggered by the Magnitude 7.3 Landers, California, Earthquake. *Science* **260** (5114), 1617–1623.

JAEGER, H. M., LIU, C.-H. & NAGEL, S. R. 1989 Relaxation at the Angle of Repose. *Physical Review Letters* **62** (1), 40–43.

Jaeger, H. M, Liu, C.-H., Nagel, S. R & Witten, T. A 1990 Friction in Granular Flows. *Europhysics Letters (EPL)* **11** (7), 619–624.

Jean, M. 1999 The non-smooth contact dynamics method. *Computer Methods in Applied Mechanics and Engineering* **177** (3-4), 235–257.

Jean, Michel & Moreau, J. J. 1992 Unilaterality and dry friction in the dynamics of rigid body collections. In *1st Proceedings of Contact Mechanics International Symposium*, pp. 31–48. Lausanne, Switzerland: Presses Polytechniques et Universitaires Romandes.

Jia, X., Brunet, Th. & Laurent, J. 2011 Elastic weakening of a dense granular pack by acoustic fluidization: Slipping, compaction, and aging. *Physical Review E* **84** (2), 020301.

Jia, X., Caroli, C. & Velicky, B. 1999 Ultrasound propagation in externally stressed granular media. *Phys. Rev. Lett.* **82**, 1863–1866.

Johnson, D. L., Schwartz, L. M., Elata, D., Berryman, J. G., Hornby, B. & Norris, A. N. 1998 Linear and Nonlinear Elasticity of Granular Media: Stress-Induced Anisotropy of a Random Sphere Pack. *Journal of Applied Mechanics* **65** (2), 380–388.

Johnson, K. L. 2014 Contact Mechanics. In *Plasticity*, pp. 404–455. CRC Press.

Johnson, P. A. & Jia, X. 2005 Nonlinear dynamics, granular media and dynamic earthquake triggering. *Nature* **437** (7060), 871–874.

Johnson, P. A., Savage, H., Knuth, M., Gomberg, J. & Marone, C. 2008 Effects of acoustic waves on stick–slip in granular media and implications for earthquakes. *Nature* **451** (7174), 57–60.

Keefer, D. K. 2002 Investigating landslides caused by earthquakes - A historical review. *Surveys in Geophysics* **23** (6), 473–510.

Khidas, Y. & Jia, X. 2010 Anisotropic nonlinear elasticity in a spherical-bead pack: Influence of the fabric anisotropy. *Phys. Rev. E* **81**, 021303.

Lastakowski, H., Géminard, J.-C. & Vidal, V. 2015 Granular friction: Triggering large events with small vibrations. *Scientific Reports* **5** (1), 13455.

Leibig, M. 1994 Model for the propagation of sound in granular materials. *Phys. Rev. E* **49**, 1647–1656.

Lemrich, L., Carmeliet, J., Johnson, P. A., Guyer, R. & Jia, X. 2017 Dynamic induced softening in frictional granular materials investigated by discrete-element-method simulation. *Phys. Rev. E* **96**, 062901.

Léopoldès, J., Conrad, G. & Jia, X. 2013 Onset of Sliding in Amorphous Films Triggered by High-Frequency Oscillatory Shear. *Physical Review Letters* **110** (24), 248301.

Leópoldès, J., Jia, X., Tourin, A. & Mangeney, A. 2020 Triggering granular avalanches with ultrasound. *Physical Review E* **102** (4), 042901.

Liu, C. & Nagel, S. R. 1992 Sound in sand. *Phys. Rev. Lett.* **68**, 2301–2304.

Makse, H. A., Gland, N., Johnson, D. L. & Schwartz, L. 2004 Granular packings: Nonlinear elasticity, sound propagation, and collective relaxation dynamics. *Phys. Rev. E* **70**, 061302.

Mangeney, A., Roche, O., Hungr, O., Mangold, N., Faccanoni, G. & Lucas, A. 2010 Erosion and mobility in granular collapse over sloping beds. *Journal of Geophysical Research: Earth Surface* p. 1–21.

Marone, C. 1998 LABORATORY-DERIVED FRICTION LAWS AND THEIR APPLICATION TO SEISMIC FAULTING. *Annual Review of Earth and Planetary Sciences* **26** (1), 643–696.

Martin, H. A., Mangeney, A., Lefebvre-Lepot, A., Maury, B. & Maday, Y. 2023*a* An Optimization-Based Discrete Element Model for Dry Granular Flows: Application to Granular Collapse on Erodible Beds. *Journal of Computational Physics* **498** (September 2022), 112665.

Martin, H. A., Peruzzetto, M., Viroulet, S., Mangeney, A., Lagrée, P.-Y., Popinet, S., Maury, B., Lefebvre-Lepot, A., Maday, Y. & Bouchut, F. 2023*b* Numerical simulations of granular dam break: Comparison between discrete element, Navier-Stokes, and thin-layer models. *Physical Review E* **108** (5), 054902.

Maury, B. 2006 A time-stepping scheme for inelastic collisions: Numerical handling of the nonoverlapping constraint. *Numerische Mathematik* **102** (4), 649–679.

Melosh, H. J. 1996 Dynamical weakening of faults by acoustic fluidization. *Nature* **379** (6566), 601–606.

Moreau, J. J. 1988 Unilateral contact and dry friction in finite freedom dynamics. In *Nonsmooth Mechanics and Applications* (ed. Jean-Jacques Moreau & P. D. Panagiotopoulos), pp. 1–82. Vienna: Springer.

Moreau, Jean Jacques 1994 Some numerical methods in multibody dynamics : application to granular materials. *European Journal of Mechanics - A/Solids* **13**, 93–114, `https://hal.science/hal-01789082/`.

Moreau, J. J. 1999 Numerical aspects of the sweeping process. *Computer Methods in Applied Mechanics and Engineering* **177** (3-4), 329–349.

Moreau, Jean Jacques 2004 An introduction to Unilateral Dynamics. In *Novel Approaches in Civil Engineering* (ed. Michel Frémond & Franco Maceri), , vol. 14, pp. 1–46. Berlin Heidelberg: Springer.

MOSEK APS 2010 The MOSEK optimization software. Available at: http://www.mosek.com, accessed: 09/11/2023.

Nasuno, S., Kudrolli, A. & Gollub, J. P. 1997 Friction in Granular Layers: Hysteresis and Precursors. *Physical Review Letters* **79** (5), 949–952.

Parteli, E. J. R., Gomes, M. A. F. & Brito, V. P. 2005 Nontrivial temporal scaling in a Galilean stick-slip dynamics. *Physical Review E* **71** (3), 036137.

Pouliquen, O. & Renaut, N. 1996 Onset of Granular Flows on an Inclined Rough Surface: Dilatancy Effects. *Journal de Physique II* **6** (6), 923–935.

Quartier, L., Andreotti, B., Douady, S. & Daerr, A. 2000 Dynamics of a grain on a sandpile model. *Physical Review E* **62** (6), 8299–8307.

Radjai, Farhang & Richefeu, Vincent 2009 Contact dynamics as a nonsmooth discrete element method. *Mechanics of Materials* **41** (6), 715–728.

Scholz, C. H. 2019 *The Mechanics of Earthquakes and Faulting*. Cambridge, UK: Cambridge University Press.

SCoPI software 2022 The scopi software. Availabel at: http://www.cmap.polytechnique.fr/~lefebvre/SCoPI/index.html, accessed: 02/07/2024.

Seguin, A, Lefebvre-Lepot, A, Faure, S & Gondret, P 2016 Clustering and flow around a sphere moving into a grain cloud. *The European Physical Journal E* **39** (6), 63.

Somfai, Ellák, Roux, Jean-Noël, Snoeijer, Jacco H., van Hecke, Martin & van Saarloos, Wim 2005 Elastic wave propagation in confined granular systems. *Physical Review E* **72** (2), 021301.

Staron, L. & Hinch, E. J. 2005 Study of the collapse of granular columns using two-dimensional discrete-grain simulation. *Journal of Fluid Mechanics* **545**, 1–27.

Tang, Hongxiang, Song, Rui, Dong, Yan & Song, Xiaoyu 2019 Measurement of restitution and friction coefficients for granular particles and discrete element simulation for the tests of glass beads. *Materials* **12** (19), 3170.

Tasora, A., Negrut, D. & Anitescu, M. 2008 Large-scale parallel multi-body dynamics with frictional contact on the graphical processing unit. In *Proceedings of the Institution of Mechanical Engineers, Part K: Journal of Multi-body Dynamics*, , vol. 222, pp. 315–326.

van den Wildenberg, S., van Hecke, M. & Jia, X. 2013 Evolution of granular packings by nonlinear acoustic waves. *Europhysics Letters* **101** (1), 14004.

www.engineeringtoolbox.com 2022 The Engineering Toolbox. https://www.engineeringtoolbox.com/friction-coefficients-d_778.html.

Wyart, M. 2009 On the dependence of the avalanche angle on the granular layer thickness. *EPL (Europhysics Letters)* **85** (2), 24003.

Zaloj, V., Urbakh, M. & Klafter, J. 1999 Modifying Friction by Manipulating Normal Response to Lateral Motion. *Physical Review Letters* **82** (24), 4823–4826.